Studies of Degradation from Flooding and Current Distribution in a Self-Draining Channel-less Fuel Cell

Sharonmoyee Goswami
April 14th, 2009
Advised by Professor Jay Benziger

Submitted in partial fulfillment of the requirements for the degree of
Bachelor of Science in Engineering

Department of Chemical Engineering and Material Science and
Engineering and Engineering Biology Certificate Programs

Princeton University
I hereby declare that I am the sole author of this thesis.

I authorize Princeton University to lend this thesis to other institutions or individuals for the purpose of scholarly research.

Sharonmoyee Goswami

I further authorize Princeton University to reproduce this thesis by photocopying or by other means, in total or in part, at the request of other institutions or individuals for the purpose of scholarly research.

Sharonmoyee Goswami

Princeton University requires the signatures of all persons using or photocopying this thesis. Please sign below and give address and date.

To my family, for always being there for me.

Acknowledgments

Many thanks to my advisor, Professor Jay Benziger and the graduate students in our lab, Erin Kimball, May Jean Cheah and Qiao (Josh) Zhao. This work could not have been accomplished without the help of Nan Yao, Director of the PRISM Imaging and Analysis Center and Gerald Poirier at the IAC. Thanks to Professor Link for the use of his ultrasonicator.

This thesis was funded by the Lidow Senior Thesis Fund and the Rudlin Senior Thesis Fund.

Abstract

The recent wave of interest in sustainability has brought the benefits of fuel cells into the public sphere. Polymer electrolyte membrane fuel cells provide clean and renewable energy, but are subject to degradation. Given the possibilities for use in remote applications, it is necessary to understand and minimize degradation of fuel cell components. Here we analyze common types of degradation resulting from flooding and unusual current distributions in self-draining channel-less fuel cells. Using scanning electron microscopy and energy dispersive x-ray analysis, we show that both flooding and aberrant current distributions do increase the rate of degradation of the membrane electrode assembly. In addition, the current distributions at the anode and cathode are initially equivalent, but anode currents are much more sensitive to small perturbations to the system than the cathode, except in cases of flooding. This suggests that the cathode reaction sites are inherent properties of the membrane electrode assembly structure. If these systems are implemented, the disconnection of a single pillar or equivalent could lead to failure. Furthermore, particular orientations are more susceptible to flooding using this design. If these two characteristics increase degradation rate, improved water removal and stability systems may need to be added to maximize performance of this fuel cell design.

Table of Contents

Table of Figures

1. Introduction

The dual concerns of global warming and dependence on foreign sources for energy has spurred national action towards finding clean and renewable energy alternatives. Fuel cells produce usable energy from hydrogen and oxygen while yielding only water as a byproduct, thus providing clean and renewable energy option. Although there are many fuel cell types, polymer electrolyte membrane fuel cells (PEMFCs) fit best within the current energy infrastructure because of their low operating temperatures, high power density, and energy efficiency[1].

Recently, much effort has been directed towards optimizing catalysts, membranes and gas diffusion layers (GDLs) and combining them to create improved membrane electrode assembles (MEAs). As prototypes near targets for field testing, the research and development focus has shifted to examining degradation of materials[2]. Many of the possible uses for fuel cells involve remote applications, including unmanned aerial vehicles, small autonomous robot vehicles, unattended ocean sensors and transponders[1]. Since part replacement is significantly more difficult in these cases, minimizing degradation is key. Degradation is frequently associated with undesired oxidation reactions that occur when gas and liquid water co-exist in flow channels or in the GDL. For the scope of this research, the water accumulation effects on material degradation in the cell will be the primary focus. Water management itself is a significant engineering challenge since the hydration state of the MEA must be controlled for optimal operation. When working with dry feeds, flow fields must be properly structured such that the water produced in the cell can mix with the dry reactant gas feeds. This has been accomplished using a channel-less flow field that promotes back-mixing to allow operation at 115°C with dry feeds at 2 bar[3]. In contrast, serpentine or parallel flow channel designs require humidification to operate at elevated temperatures because of drying fronts.

Despite water management, liquid water condensation in PEMFCs creates fluctuations in the current and voltage output. This suggests that the assumption of uniform corrosion in the fuel cell is

invalid. In support of this claim, it has been shown that water accumulates in corners and in areas of the flow channels from gravity[4], and segmented anode studies have shown that liquid drops and slugs form periodically at the same location and grow until they are pushed from the channel[5-7]. When these drops block the gas flow, downstream current can decrease from reactant starvation at the membrane-electrode interface. A secondary focus of this research is to determine the characteristic flow patterns in the self-draining fuel cell and use these to predict resulting degradation from varying current distributions.

2. Goals

This thesis examines the effects of water flooding on the local current density in parts of the electrode, which leads to lateral potential variations. These potential variations can contribute to corrosion by starving parts of the MEA of reactant gases. The amount of corrosion is measured using a combination of scanning electron microscope images (SEM) and element maps using energy dispersive x-ray analysis (EDX), a recommended *ex situ* method of testing cell durability[8]. This corrosion is quantified by the amount of carbon support that was degraded and/or the amount of platinum that was dissolved or sintered. The amount of corrosion is also compared to the effective potentials at the electrode during operation using the model developed by Chia et al.[9]

3. Background

3.1 Fuel Cell Operation and Materials

The PEMFCs used for this work operate at room temperature. The majority of PEMFCs use Nafion membranes which are impermeable to gas diffusion, possess a higher acidity and are more stable than alternative membranes. Nafion consists of a hydrophobic backbone that has a polytetrafluoroethylene structure (PTFE, Teflon) with hydrophilic sulfonic acid side groups.

The two main reactions in the fuel cell are as follows[10]:

$$O_2 + 4H^+ + 4e^- \rightarrow 2H_2O \qquad E_o = 1.229 \text{ V (Cathode)} \qquad 3.1.$$

$$H_2 \rightarrow 2H^+ + 2e^- \qquad E_o = 0 \text{ V (Anode)} \qquad 3.2.$$

The conductivity of the membrane allows the protons to travel across the membrane from the anode to the cathode, allowing the above reactions to take place. Membranes are usually water filled to maintain high conductivity in the sulfonic acid membranes. Water in its liquid or gaseous form is a product of the reactions at the cathode as seen in reaction (3.1); however, there is some diffusion of water within the cell.

A characteristic cell MEA comprises a carbon-supported noble metal catalyst such as platinum, an ionic conductor such as Nafion, and a water repelling agent such as Teflon. The purpose of each of these components is discussed below.

The electrodes in PEMFCs ensure the supply of the reactant gases to the active zones where the catalyst is in contact with the ionic and electronic conductor. In the experiments discussed here and in much of literature, fuel cells use noble metal catalysts on high surface area carbon as the active catalyst layers[11]. The carbon support enables the uniform dispersion of platinum nanoparticles, retards the sintering or agglomeration of these particles, and provides electronic continuity[10]. The dispersed platinum nanoparticles form the thin catalyst layer on the carbon surface, typically with a platinum loading on the order of 0.4-0.6 (mg/cm^2) [12-14].

The catalyst layer is where the electrochemical reaction takes place. There are three kinds of species that participate in this reaction: gases, electrons, and protons, which must all be present for the reaction to occur[1]. Electrons travel through the conductive catalyst and carbon support, protons through the ionomer, and the gas through the electrode pores. Thus, the catalyst particle on the carbon support, the ionic conductor and the gas (reactant) supply come together at the three phase boundary (Figure 1).

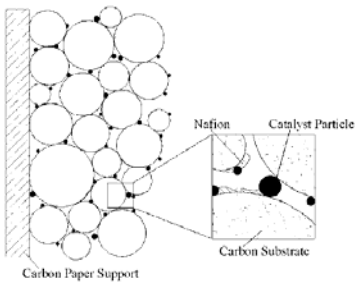

Figure 1. Three Phase Boundary Diagram of three-phase boundary desired in membrane electrode assembly

This three phase boundary is created by impregnating the catalyst/support with an ionomeric binder before pressing the electrode onto the membranes. This ensures that most catalyst particles are in contact with ionomer chains that have an ionic connection with the membrane. Studies have shown that applying solubilized Nafion in a mixture of alcohols increases the active surface area and reduces the charge transfer resistance per square centimeter[15].

Finally, the reactant gases diffuse through the GDL and the carbon support to the catalyst particles. When the fuel cell uses humidified gases, the GDL must be sufficiently hydrophobic to prevent flooding of the pores. This is accomplished through the introduction of a water repelling agent. The GDL typically consists of carbon cloth (woven carbon fibers) or carbon paper (pressed carbon fibers). The former has 3-5 fold higher gas permeation rates, although the latter provides increased stability and stiffness. Carbon cloth electrodes were used for all experiments described in this work. Adding a surface layer known as the microporous layer (MPL) onto the ordinary substrate layer has been shown to improve water and gas management of the whole GDL structure[14]. This MPL consists of carbon or graphite particles mixed with a hydrophobic agent such as PTFE that acts as a binder. The difference between the MPL and the GDL comes from differences in pore size, since the MPL has pores between 100-500 nm and the GDL has pores between 10-30 μm[14, 16].

3.2 Mechanisms of Membrane Electrode Assembly Degradation

Degradation of fuel cell components significantly reduces the lifetime of the overall cell. There are multiple degradation mechanisms, including cathode catalyst degradation from particle sintering and catalyst support corrosion[17]. Here we discuss degradation mechanisms for each main fuel cell component.

3.2.1 Carbon Support Degradation

Although carbon supported catalysts are more stable than non-supported catalysts in preventing catalyst agglomeration during cell operation[18], degradation can still occur. Carbon is oxidized at potentials near the open circuit voltage of a fuel cell (1.0 V), and this oxidation rate increases with the potential. Carbon support oxidation has been shown to occur during start-up and shut-down conditions in proton exchange membrane fuel cells, when a H_2 front displaces air in the anode compartment after long shutdown periods and momentarily increases the local cathode potential to much higher values (0.6-1.4 V)[19]. At this potential, the carbon support may corrode completely in a few hours. Other corrosive conditions include high water content, low pH (<1), high temperature (50-90°C), and high oxygen concentration[17]. The principal reaction to describe electrochemical oxidation of carbon in aqueous solutions is[20]:

$$C + 2H_2O \rightarrow CO_2 + 4H^+ + 4e^- \qquad 0.207\ V \qquad 3.3.$$

These degradation patterns have been previously observed in cells operating at 80°C, 100% relative humidity and 150 kPa. Fortunately, this reaction has relatively slow kinetics, allowing the use of carbon in fuel cells. Similarly, it has been shown that on Vulcan XC-72, carbon surface oxidation occurs at 65°C and 0.8V. This mechanism is related to local hydrogen starvation[19].

This work explores whether a similar starvation situation can arise from the presence of liquid water. Liquid water creates mass transport resistance for reactants to get to the MEA, which both reduces local current density and leads to local lateral potential variations that contribute to corrosion. It is not clear if these lateral potential variations can increase local potentials to corrosive levels. Conversely, lateral currents can also arise when the local water concentration is depleted, since higher membrane resistance causes currents to bypass high resistance areas. Drying fronts from this phenomenon have been previously observed[7]. These fronts can incite degradation and lead to failure of the cell.

Furthermore, in all of these corrosive situations, the presence of platinum could accelerate the carbon corrosion rate. The role of platinum in carbon support corrosion has been previously tested with carbon supported catalysts samples held at moderate temperatures (125-195°C) under dry air conditions[11]. These tests showed that platinum particles could catalyze the combustion of the carbon support, and that net corrosion is more severe in locations where the platinum particles reside. This leads to weakened attachment between the platinum particles and the carbon support, leading to faster platinum particle agglomeration[21]. The presence of platinum has a consistent effect on carbon corrosion at ordinary operating voltages of 0.4-0.7V, but is more significant when portions of the cell experience higher potentials, causing the carbon support to rapidly corrode[19]. The altered carbon oxidation reactions with platinum catalysts are as follows[20]:

$$C + H_2O \rightarrow CO_{surf} + 2H^+ + 2e^- \qquad (>0.3\ V) \qquad 3.4.$$

$$CO_{surf} + H_2O \xrightarrow{Pt} CO_2 + 2H^+ + 2e^- \qquad 0.8\ V \qquad 3.5.$$

This corrosion has been found to significantly reduce overall fuel cell performance[21]. In addition to this performance drop, studies have shown that degradation of the carbon support is manifested in other quantifiable ways. For example, CO_2 emissions from Pt/C catalysts were higher than in carbon-only electrodes, although this effect was less pronounced at temperatures above 50°C[22]. The importance of water effects are reinforced by evidence suggesting that carbon degradation increases under humidified conditions[23].

3.2.2 Platinum Catalyst Degradation

In addition to corrosion of the carbon support, studies have also shown degradation of the platinum catalyst itself. The reduction of active platinum surface area is accelerated if the electrode potential is continuously cycled between oxidizing and reducing conditions, which best mimic the real-life operating conditions[24]. The degradation is more pronounced in the cathode, because the oxygen reduction reaction has much slower kinetics than the H_2 oxidation of the anode side[9]. This

reduction reaction can be visualized by examining the growth of platinum particles and dissolution of platinum in the membrane phase[12].

Major platinum area losses occurring due to dynamic operating conditions lead to significant performance losses similar to those seen with carbon corrosion. This follows from the fact that the electrocatalytic properties of platinum are dependent on crystallite size and a change in platinum surface area is expected to result in a performance loss[25]. A kinetic model for this oxidation and dissolution has been proposed, using the following electrochemical reactions[26]:

Platinum dissolution

$$Pt \rightarrow Pt^{2+} + 2e^- \qquad 1.188\ V \qquad (3.6.)$$

Platinum oxide film formation

$$Pt + H_2O \rightarrow PtO + 2H^+ + 2e^- \qquad 0.980\ V \qquad (3.7.)$$

Platinum combustion at the cathode

$$2Pt + O_2 \rightarrow 2PtO \qquad (3.8.)$$

The oxidation of platinum was observed at potentials as low as 0.6V, and Pt^{2+} ion concentration increases most rapidly at 1.1V[26]. However, it has been found that platinum stability reaches a peak at intermediate potentials, around 0.95V at the cathode. This supports that startup and shutdown conditions exacerbate corrosion. Platinum particle growth during fuel cell operation has been observed and leads to decreased catalyst surface area. Similarly, previous experiments have shown that the catalyst particle size distribution shifted during operation, increasing from 3 nm to 4 nm in only 300 hrs and to 5 nm after 4000 hours with a current density of 1.5 A/cm^2 at 100°C[25]. The underlying mechanism of platinum area loss in the cathode is based on the Ostwald ripening mechanism on the carbon support and platinum precipitation in the ionomer phase.

3.2.3 Gas Diffusion Layer and Microporous Layer Degradation

As discussed earlier, the GDL and MPL are responsible for gas phase transport, electronic contact, heat removal and water removal. Although the carbon in the catalytic layer can corrode, the

carbon black in the MPL is not susceptible to electrochemical corrosion and does not contain platinum to catalyze oxidation reactions. However, surface oxidation from contact with water during flooding and loss of carbon via oxidation to CO and CO_2 has been seen in earlier experiments[27]. In some cases, the hydrophobic coatings used in the GDL and MPL have also undergone losses from decomposition[28]. These latter degradation mechanisms caused the GDL and MPL to lose their hydrophobic character, changing the pore structure of the materials. This degradation has been shown to increase the water content of the GDL and MPL and thereby block gas phase mass transport through the pores.

3.3 Flooding Effects and Modeling

In preparation for the examination the effects of flooding on electrode degradation, typical patterns of water flow and water management were studied. PEM fuel cells operate below the boiling point of water and thus allow condensation that may restrict gas delivery or block the catalyst active area[4]. This build-up of water is referred to as flooding.

The modeling of flooding effects at the cathode will be accomplished by using relationships previous presented by this lab[9]. Flooding causes water to accumulate within the catalyst layer of the GDL, creating additional mass transport resistance for the O_2 gas in the chamber. In an ideal fuel cell, there would be no flooding to block mass transfer allowing for a mass transfer coefficient at the cathode, k_c^{max} of 5.8 × 10^{-7} mol/m^2-s-Pa. With liquid water formation, this mass transfer can approach a smaller minimum rate coefficient, k_c^{min} of 5.8 × 10^{-10} mol/m^2-s-Pa. This relationship between mass transfer coefficient and water formation is shown in equation (3.9); where n_w^{max} indicates the maximum moles of water that can be contained at the CL/GDL interface and n_w^L represents the moles of liquid water present in the GDL:

$$k_c = \frac{k_C^{max}}{1 + \frac{n_w^L}{n_w^{max}}\left(\frac{k_C^{max} - k_C^{min}}{k_C^{min}}\right)} \qquad 3.9.$$

There are additional parameters that are affected by the conditions in the fuel cell. For example, at steady state, the rate of mass transfer to the catalyst is equal to the rate of reaction at the catalyst surface. As a result, the reactant partial pressures at the electrode-electrolyte interface are reduced relative to those partial pressures within the flow field due to mass transfer across the GDL. Using the values for k_c calculated from 3.8 and estimated values for k_a of 5.8 × 10^{-6} mol/m^2-s-Pa, these new pressure values can be calculated from local currents (i) using equations 3.10 and 3.11:

$$P_{H_2}^{cat} = P_{H_2} - \frac{i}{2Fk_aA} \quad 3.10.$$

$$P_{O_2}^{cat} = P_{O_2} - \frac{i}{4Fk_cA} \quad 3.11.$$

where F represents Faraday's constant, and A is the cross-sectional area of the GDL.

Since the fuel cell will be only partially flooded at any given time, the effective fuel cell voltage may be calculated to determine if corrosive conditions are present. By treating the electrochemical reactions at the anode and cathode as chemical diodes and applying typical Butler-Volmer kinetics, the local potential difference (V_{FC}) can be determined from the local current (i)[9] through the following relationship:

$$V_{FC} = V_o - V_T\left(1 + \frac{i}{I_o}\right) + \frac{RT}{4F} ln \frac{\left(P_{H_{2,anode}}^{cat}/P_T\right)^2\left(P_{O_{2,cathode}}^{cat}/P_T\right)}{a_{gdl}^2} \quad 3.12.$$

where V_o is the thermodynamic potential at standard conditions, P_T is the total pressure in the flow region, V_T is the diode threshold voltage, I_o is the diode saturation current and a_{gdl} is the water activity in the GDL.

4. Experimental Methods

In the PEMFCs used for these experiments, the flow fields were specifically designed to measure local current density with the ability to independently measure electrode corrosion and membrane-electrode assembly degradation under well-defined conditions. The fuel cell and the procedure shown here is adapted from Kimball et al[7].

The fuel cell tests were completed using a self-draining channel-less fuel cell. The cell used consisted of two polycarbonate plates flanked by aluminum plates on the outside, with each set of polycarbonate and aluminum plates in the arrangement shown in Figure 2A.

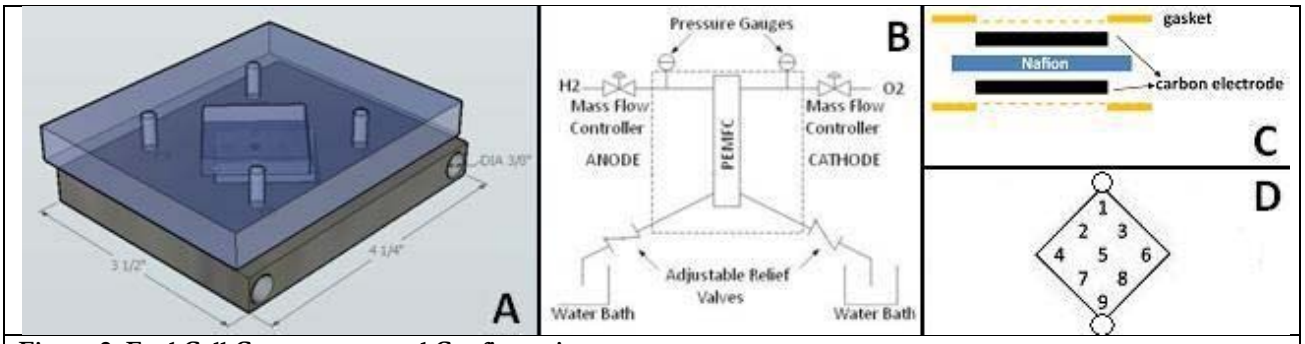

Figure 2. Fuel Cell Components and Configuration:
A. Polycarbonate plate with diamond cut from center. In this diamond region, nine screws are placed to create a distributed electrode for current contact. Beneath the polycarbonate plate is an aluminum plate of the same size. These two plates are bonded to one another before use. The fuel cell is created from placing an MEA between two polycarbonate plates, flanked by two aluminum plates. The cell is then secured by inserting screws in the locations shown. **B**. The fuel cell structure described in (A) is placed into the system shown here at PEMFC with co-current inlet gas flows and outlet flows as shown. The dashed line denotes the system boundary. **C**. Order of components in MEA. Platinum is on the carbon electrode surface for process A and on the Nafion membrane surface for process B. The dotted lines on the gasket image indicate that a diamond is cut from the center of the silicon gasket to match that on the polycarbonate plate. The carbon electrode is the size of the diamond region, whereas the Nafion membrane extends ¼" beyond the electrode on each side. **D**. Labeling and placement of the screws in the distributed electrode of the gas plenum region described in (A). In this configuration, (1-9) are labeled, with "A" denoting the anode side and "C" denoting the cathode side.

The MEA is placed between the two polycarbonate plates. A 3.175 cm × 3.175 cm diamond was cut out from the center of each polycarbonate plate to create a gas plenum or gas mixing region, with nine 4/40 screws for current collection in the locations shown in Figure 2D. The anode and cathode flow regions were on the same plane and terminated at a 90° angle that connected to a tube fitting adapted to 1/8" PTFE tubing at the top and bottom of the diamond flow regions, (1) and (9), respectively. The top tubing connected to inlet and the bottom tubing to the outlet mass flows. The lead wires from each screw connected individually to a 0.1 Ω sensing resistor, R_{sense}. The nine leads from the sensing resistors on the anode were connected together and a common lead was connected through a 0-20 Ω, 10 turn potentiometer to the common lead from the nine sensing resistors on the cathode side. This fuel cell was operated with an external load resistance of 0.5 Ω for the experiments described here.

A computer data acquisition board, interfaced using LabView, read the voltage drops across the load as well as across each sensing resistor. The tubing from the gas flow channel outlets were bled into 10 mL graduated cylinders with a small hydrostatic head (~2-3 cm H_2O) to maintain the cell pressure at 1 bar. This ensured that reactant gases did not back diffuse into the flow channels. This full apparatus is shown in Figure 2B. Gas bubbles leaving the cathode and anode were also seen in the cylinders, allowing visual identification of reactant excess or leakage. All the results reported here are for fuel cell operation at 20-25°C; the vapor pressure of water is sufficiently low (~0.025 bar) such that convection of water vapor is negligible, and all water transport is by liquid flow.

4.1 Method for Constructing Membrane Electrode Assembly

Two MEA constructions were used in these experiments. For the preliminary study, the MEAs used were constructed using Nafion 115 membranes with dimensions of 4.45 cm × 4.45 cm, carbon cloth GDLs, and silicon gaskets. The GDLs used were ELAT V2.1 Carbon Cloth (BASF Fuel Cell, Somerset, NJ) with the catalyst (0.5 mg/cm^2 of 20 wt% platinum on Vulcan XC-72) applied on one side. The dimensions of the electrodes were 3.175 cm × 3.175 cm, giving a total area of 10.08 cm^2. These electrodes were first painted using 5 wt% solubilized Nafion (Ion Power, New Castle, DE) and then baked in an oven for 1 hr at 70°C. The membranes used were first cut to the requisite size and then activated by boiling in 3% H_2O_2 and 1M sulfuric acid. These activated membranes were stored in deionized water until pressing. All the components for the MEA were placed together in the order shown in Figure 2C between two sheets of Teflon. This assembly was placed in the metal press where it was heated from 70°C to 140°C. At 140°C, 2 tons of pressure was put on the assembly for 90 seconds to press it together. The MEA was removed and left to cool to room temperature to allow polymer creep to take place and create the necessary structures for fuel cell operation. Pressed MEAs were stored at 100% relative humidity until use, and will be referred to as "process A MEAs".

However, process A MEAs cannot be delaminated after use in the fuel cell. Since the degradation effects cannot be studied without delamination, a second process was adopted that did not require hot pressing[13]. The same dimensions of Nafion 115 membranes, carbon cloth GDLs, and silicon gaskets were used. The GDLs in this case were ELAT V2.1 with no catalyst added (BASF Fuel Cell, Somerset, NJ). Catalyst slurries were prepared by sonicating 275 mg ETEK 20 wt% platinum on Vulcan XC-72 (BASF Fuel Cell, Somerset, NJ) in 1.56 grams solubilized Nafion and 7 grams acetone for 30 minutes using an ultrasonicator at 0.04 rms-watts. Although the activated membranes were stored in deionized water as with process A, prior to spraying they were dried at 80°C for two hours. This ensured a flat spraying surface for uniform coverage. After the membrane was secured with an aluminum frame, the catalyst slurry was sprayed onto the Nafion surface using nitrogen as an airbrushing gas; yielding platinum coverage of 0.5 mg/cm^2 and ionomer concentration of 0.7 mg/cm^2, as recommended[29]. This catalyst coated membrane was dried between sheets of polypropylene at 80°C for 15 minutes. The remaining structure in Figure 2D was assembled within the fuel cell structure itself at 25°C. MEAs created by this process are referred to as "process B" MEAs.

4.2 Fuel Cell Configuration and Operation

Each of the following experiments have been completed using a self-draining, channel-less fuel cell using stoichiometric flow rates of 3.5 sccm O_2 and 7 sccm H_2 and a load resistance of 0.5 Ω at 20-25°C. As with earlier experiments, there is variability in the internal resistance among MEAs, particularly between process A and process B MEAs. The variance in current values from variable internal resistance remained within 10%. To best approximate configurations that lead to varying degradation profiles, four main orientations were used: (1) Vertical Configuration I, (2) Vertical Configuration II, (3) Horizontal Configuration I and (4) Horizontal Configuration II. Regardless of orientation, the inlet gas flows were always co-current for the data presented here, reactant gases

enter at segment (1) and product water exits at segment (9). In a position referred to as Vertical Configuration I, the inlet flows are at the top of the cell and in the direction of gravity such that both inlet flow and water drainage are gravity-assisted. Region (1) is at the highest point, whereas region (9) is at the lowest point. This position is the self-draining orientation. In a second position referred to as Vertical Configuration II, the reactant inlet flows are against gravity. Region (1) is at the lowest point and region (9) is at the highest point.

For this research, only two of the three possible horizontal orientations were tested. This modification was made based on previous observations[7] that fuel cells oriented with the cathode below the anode and with the two electrodes on the same plane behave identically. In Horizontal Configuration I, the fuel cell is on its side such that the cathode and anode are on the same plane. In this orientation, region (4) is at the highest point and region (6) is at the lowest point in the cell. In Horizontal Configuration II, the fuel cell is on its side such that the anode is on a lower plane than the cathode. In this orientation, all of the locations on each electrode are at the same height. All MEAs maintained the same side used as the cathode and as the anode for the entire period of operation.

After use, each MEA was removed from the cell and cut with a razor blade to divide the electrode into nine sections mirroring the regions shown in Figure 2D. Each of these subsections was divided into two, one for the anode side (labeled as 1 A for the top electrode), and one for the cathode side (labeled as 1 C for this same location). For each orientation, current-voltage (IV) curves were obtained, and were used to determine which regions are actually flooded without taking the cell apart or by visual inspection. After the cells had run for at least 24 hours, the current and voltage were measured as the external load resistance was increased from the lowest setting (~0.015 Ω) by 0.5 Ω every fifteen seconds to produce these curves. This speed is rapid enough to minimize the effects of changing water content on the membrane[6]. These same segments that are shown to

have flooded using this technique were starved for hydrogen[5, 7, 19, 21] and may be correlated with EDX maps for corrosion. Furthermore, images have been taken to visually observe any possible flooding.

5. Results and Discussion

5.1 Effect of Nafion Impregnation on Electrode Structure:

The carbon cloth electrode used in the configuration shown in Figure 2C contains a carbon-fiber bundle weave layer or GDL, a thinner MPL, and sometimes a final catalyst layer (CL). Since methods for pressing MEAs involve various processing steps prior to use in the fuel cell, it was necessary to account for any morphological effects incurred from processing. For this reason, we compared the surface of a new GDL (ELAT V2.1, 20% Pt) with one that had been impregnated with Nafion. The relative thickness of each component in the MEA is included in Appendix A.

Figure 3 shows new electrodes alongside impregnated carbon cloth electrodes. EDX mapping was used to differentiate between the carbon support, the Teflon used to induce hydrophobicity, the platinum catalyst layer and the solubilized Nafion that had absorbed on the surface (Figure 3A, B). This was accomplished by mapping carbon, fluorine, platinum and sulfur peaks.

Sulfur allows differentiation between Teflon and Nafion, since the sulfonic acid groups are not present in the Teflon polymer; however, not all of the samples showed sulfur peaks since Nafion is only present after the GDL is impregnated. In the case of multiple peaks, only the strongest peak for that element was used, since it is rarely necessary to consider all emission lines[30]. The sulfur regions in Figure 3B are in the same regions as the carbon, leading to more intensely colored bundle weaves than seen in Figure 3A. From these two images we can see that the Nafion is spread over the entire surface even on GDL layer, which is not directly impregnated. However, the Nafion impregnation step does not induce any significant structural changes on the GDL region. More striking changes are seen on the reverse side where the catalyst layer is found.

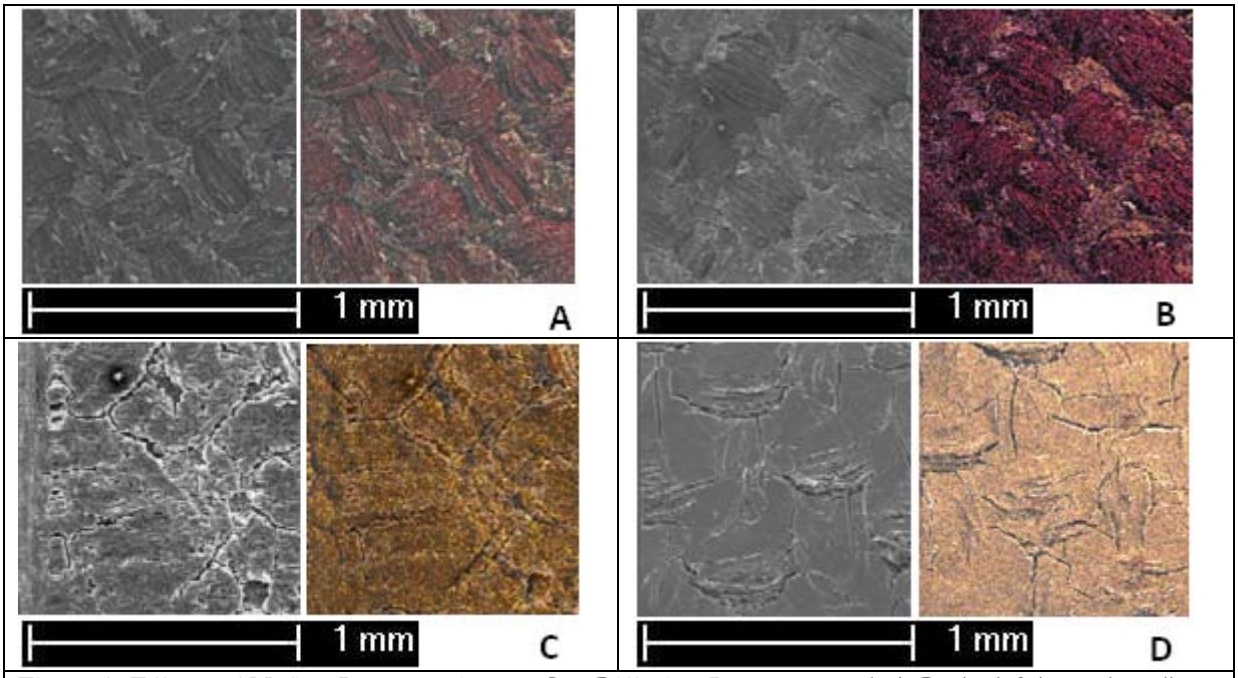

Figure 3. Effects of Nafion Impregnation on Gas Diffusion Layer: For each **A-D**, the left image is ordinary SEM image and the right image uses overlay technique to superimpose elemental maps of carbon (red) and fluorine (yellow) and occasionally sulfur (purple) and platinum (orange) onto the image. All images are at 27X magnification, 20 kV beam intensity[30], and a working distance of 10 mm. **A** and **B** show the GDL layer with carbon fiber bundle weave, **C** and **D** show the MPL/CL layer. **A** and **C** are new electrodes that have not been used, **B** and **D** are electrodes that have been impregnated with solubilized Nafion.

Figure 3C shows the surface of the MPL/CL layer prior to the impregnation step. The platinum signal is strong since the catalyst layer is on the surface of the MPL and GDL layers. On this surface, there are multiple cracks that do not appear to follow a set pattern. In contrast, in (Figure 3D), the surface consists of regular cracks that appear to share the same morphology. It is likely that the Nafion impregnation step created a smooth surface from painting, and the catalyst layer subsequently formed regular cracks upon drying.

From this analysis, we cannot tell if this is an accurate representation of the carbon layers underneath. To better understand these images and for further analysis of the original electrode structure, SEM and EDX analysis were also completed on the cross-section of a new electrode sample. Since these samples were too flexible to freeze fracture using liquid nitrogen, the electrode was embedded in conductive molding compound (Buehler Probemet) and pressed in an auto molding press (Simplemet) at 140°C. The top layer of the cross-section was then sanded using an

automatic sander. An SEM image of the cross-section of a new electrode (without Nafion impregnation) is shown in Figure 4.

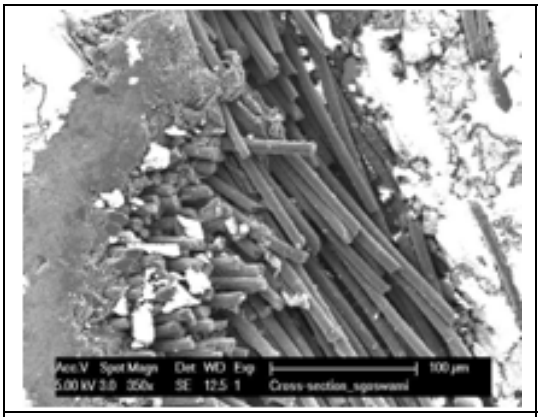

Figure 4. SEM Image of Cross-Section of ELAT V2.1 Electrode: This shows in some detail that cross-section of the electrode sample. The edges of the image are the molding compound, and on the left side we see the solid platinum catalyst surface with the carbon fibers underneath

A series of SEM images were taken at 350X along the length of the electrode sample. Measurements of the platinum surface at various locations were taken and averaged. At the thinnest point on the sample, the CL/MPL structure is approximately 62μm thick, increasing to 75μm in some locations. All of these EDX mapping experiments use a beam acceleration voltage of 20 kV through the platinum layer. This means that the maximum diffusion range beyond the surface is 0.5μm[31]. This indicates that information beyond the catalyst layer was not obtained in EDX analysis.

5.2 Membrane Surface Differences between Processes A and B

As described earlier, in order to obtain MEAs that could be delaminated, we decided to switch techniques from process A to process B. Those process A MEAs that have not been used in the fuel cell but have only been hot-pressed can be delaminated. From the following analysis, we can determine if the types of three phase contact obtained using process A and process B are of a similar nature. It is somewhat difficult to compare the surface itself, so we utilized both SEM/EDX micrographs and relevant spectra (Figure 5).

One significant difference between the micrographs seen for process A (Figure 5A) and process B (Figure 5B) is the pattern of the catalyst contact with the membrane. It appears that the variation in pressure that is applied in process A stems from the pattern of the bundle weave GDL.

As a result, the regions of the MPL/CL in process A that have the best three-phase contact are those corresponding to the center of the bundle weave, rather than the edges.

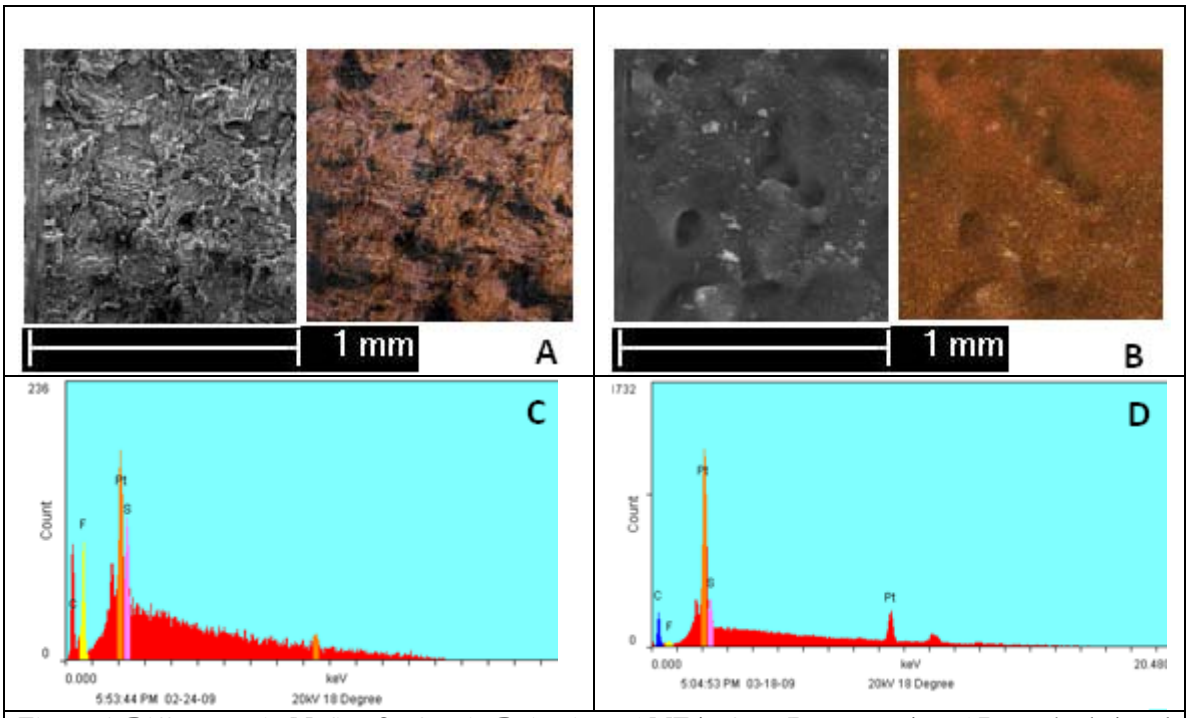

Figure 5. Differences in Nafion Surface in Delaminated MEAs from Processes A and B: For both **A** and **B**, left image is SEM micrograph of delaminated membrane at 50X, beam acceleration voltage 20 kV and a working distance of 10 mm; right image is SEM micrograph overlayed with elemental maps for carbon (red), fluorine (yellow), sulfur (purple), and platinum (orange). **C** and **D** show EDX spectra obtained for mapping. **A** and **C** show results from process **A, B** and **D** show results from process B.

In contrast, process B shows more uniform coverage of platinum, although layering effects from the airbrushing process are also present. In terms of the spectra shown in Figures 5C and 5D, the fluorine and sulfur peaks are much stronger in the process A sample. However, from comparing total currents of process A and process B MEAs, process A obtains total currents 15% higher (data not shown). However, rates of loss during airbrushing suggest that the decreased performance is from decreased coverage, rather than quality of the three-phase boundary.

5.3 Degradation at Membrane-Electrode boundary

As stated earlier, four different orientations of the self-draining channel-less fuel cell were examined to best characterize flooding effects and possible increased degradation from flooding. Two different vertical configurations of the fuel cell were examined based on the direction of gas

flow at the cathode relative to gravity. Since Vertical Configuration I is the most common and useful orientation for the cell, multiple cases were examined for this orientation only. These cases include conditions were the current was evenly distributed among the 9 regions and conditions where it was not, as well as cases where flooding affected the performance of the cell during operation.

5.3.1 Vertical Configuration I (VC-I); Gas Flow with Gravity

Regular current distribution, run for 50 hours

The long term behavior at the anode and the cathode are shown (Figure 6A, B). The colors of each cathode current match the corresponding location on the anode current; these colors will correspond to these locations for all subsequent graphs. From Figures 6A and 6B we see that the current distribution among the nine pillars is relatively constant during operation of the cell. It also appears that the current is well distributed among the electrodes that are in adequate contact with the reactant surface. Nonetheless, the standard deviation in currents at both the anode and cathode of 15 mA or 30% of average current suggests that particular reaction sites are preferred or that equal contact is not made by each pillar on the electrode surface. This latter explanation is true for electrode region (5) which does not receive the same pressure from the screws of the fuel cell as the remaining electrodes. The removal of the current values at location (5) from our time-averaged current profiles causes a significant decrease in the standard deviation from 15 mA to 10 mA.

The fuel cell system is sensitive to small perturbations, including small changes in external load resistance (i.e. 0.48 Ω to 0.5 Ω). This is seen in (Figure 6A) at 19 hours: when the anode system is tapped or similarly perturbed, the currents redistribute. At the same time the voltage and total current remain constant at 0.5 V and 1.0 A over this time period, respectively (data not shown). Although in previous studies[7] redistribution has been seen to accompany flooding, this does not appear to be the case here.

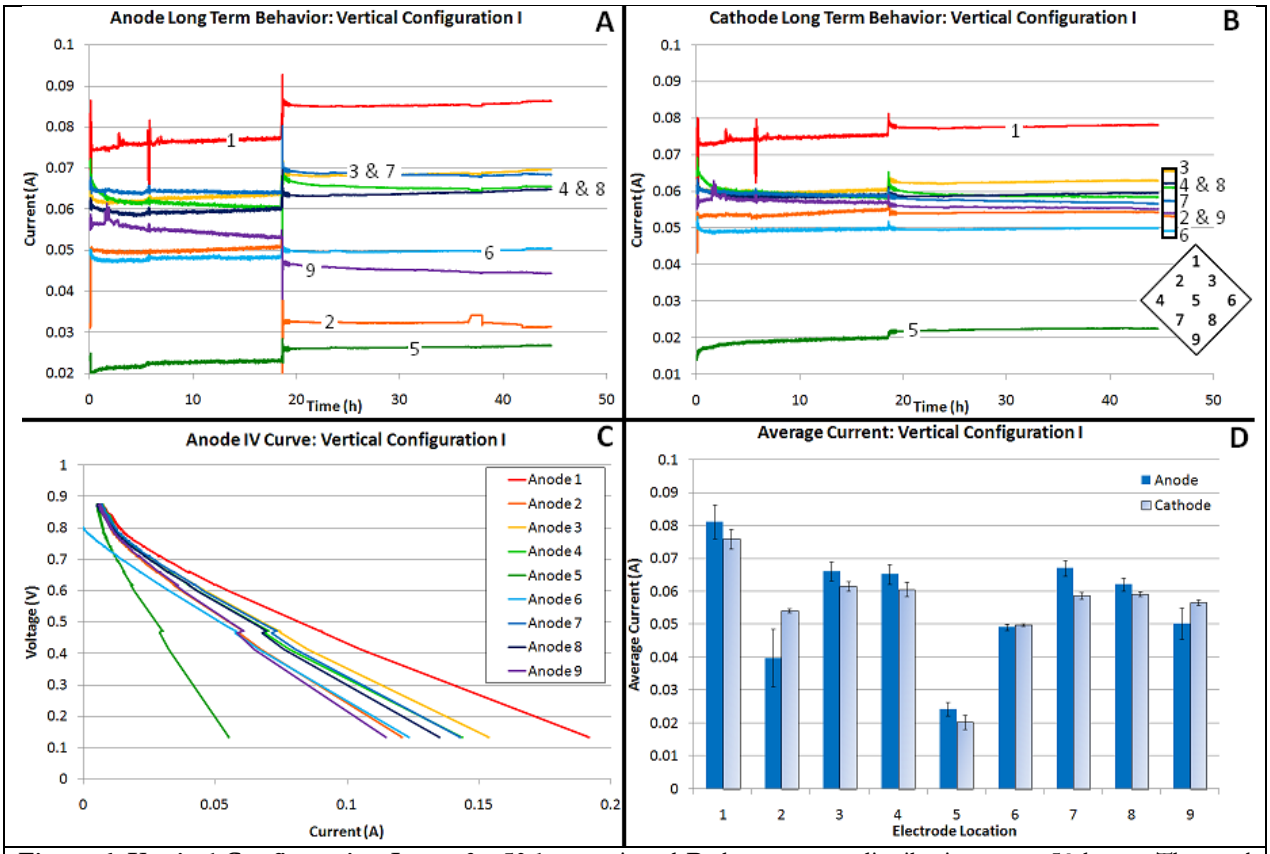

Figure 6. Vertical Configuration I, run for 50 hours: A and **B** show current distributions over 50 hours. The total current is maintained at 1.0 A and the voltage is maintained at 0.5 V (data not shown) throughout operation time. **C** shows the IV curve after 18 hour of operation, only the anode is shown since the anode and cathode curves were identical. **D** shows the time-averaged currents at the anode and cathode for all locations during operation. Total current was 1.0 A and total voltage was 0.5 V throughout operation.

Interestingly, the cathode currents are less sensitive to small perturbations. We observe that before the initial perturbation, the distribution of the currents on the anode and the cathode are almost identical. When the fuel cell is disturbed, the anode currents at locations (2) and (9) drop significantly, whereas their counterpart currents at the cathode remain constant. This is seen from the small peaks that occurred when significant current redistributions occurred on the anode side (Figure 6A, B). This suggests that cathode currents and current distributions derive from inherent reaction and flow field conditions, whereas their anode counterparts can be more easily influenced by condensation and other transient conditions. Since reaction (3.1) is takes place at the cathode, the water that is on the MEA surface is not from condensation, but from this reaction. This supports

the idea that these reaction sites will remain relatively constant despite small movements that would remove water released by condensation.

From the IV curve (Figure 6C) we can see that the flow field is not flooded at this time, indicating that there is a lower likelihood of reactant starvation in the electrode region. A flooded region would show a much lower current in comparison to the other currents, even in region (5). This information was supported visually. The IV curve at the cathode (data not shown) also demonstrated no evidence of flooding was seen, even in location (9). As the water is formed at the cathode, any flooding would impact this region first.

Using the time-averaged currents for the anode and cathode, the current distribution was plotted as a function of location (Figure 6D). The largest differences between anode and cathode behavior derive from anode current changes resulting from small perturbations, seen at location (2). Error bars on this graph denote the range of currents at this location for both the anode and the cathode. Overall, there were minimal differences seen between the anode and cathode currents.

With this information, we inspect the SEM and EDX micrographs for this anode. The images in Figure 7 show that there is little difference in the distribution of platinum and carbon on the electrode surface among the different locations on the anode. The majority of variation derives from flaking of the sprayed material, rather than from clumping of platinum from corrosion of carbon supports, as has been seen in earlier research[26]. This suggests that despite the high standard deviation of currents between electrode pillars, the currents are close enough that degradation is not accelerated in some locations relative to others. However, since there has been no flooding and thus no blocking of the anode surface, corrosion from hydrogen starvation has not yet been tested. The anode surface was also examined for oxygen peaks; however, very few peaks were obtained, and those that were recorded may have been tails from surrounding carbon and fluorine peaks[30], all

individual maps from the EDX overlay are enclosed in Appendix B. The SEM/EDX micrographs for the cathode region also do not show any effects of corrosion and are enclosed in Appendix C.

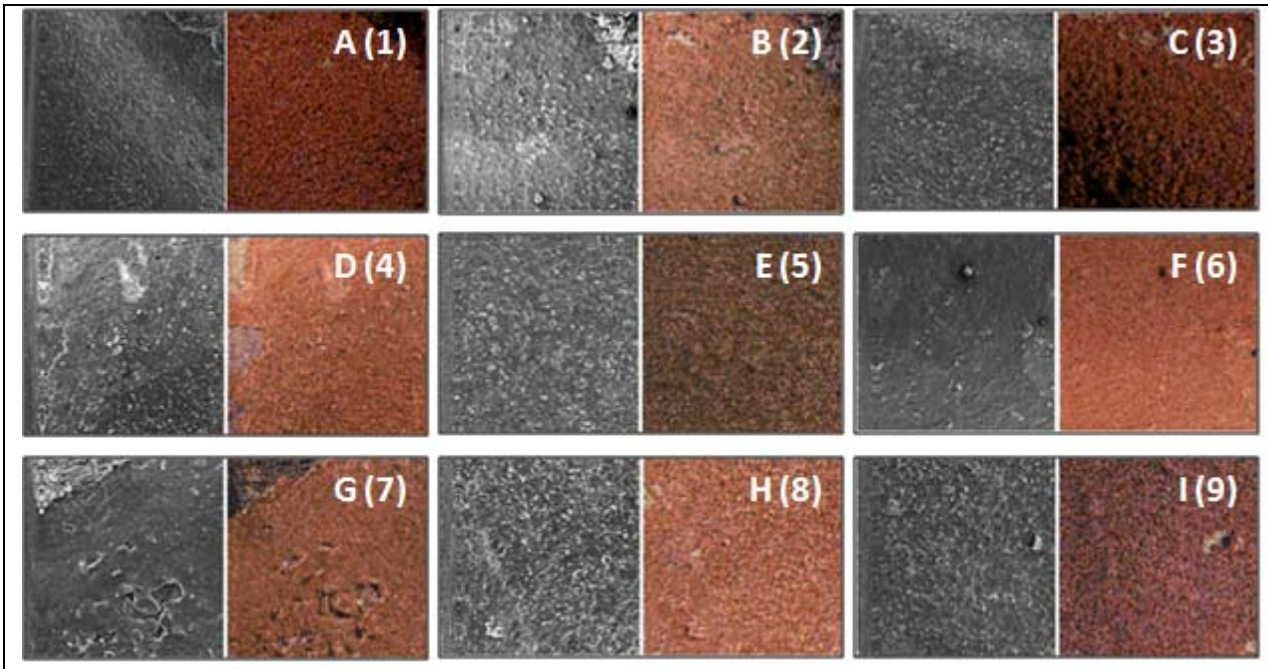

Figure 7. Anode Surface Morphology as seen in SEM/EDX Images from Vertical Configuration I, run for 50 hours: For each **A-I**, the left image shows the SEM micrograph of the anode at that region at 50X, accelerating beam voltage of 20 kV and working distance of 10 mm. The right image shows the EDX maps of carbon (red), fluorine (yellow), sulfur (purple), and platinum (copper) superimposed on the left SEM image. Supplemental information in Appendix B.

To obtain a more quantitative analysis of changes to element distribution, we also compared the relative magnitude of each peak (platinum, fluorine, sulfur) normalized using the carbon peak for each sample to the relative magnitude of each peak on an airbrushed membrane that had not been used in the fuel cell. There is some inherent error involved in this method, since there may not be equal coverage of each element in every region and debris from the gasket or other regions of the fuel cell may obscure particular areas on the sample (Figure 8).

There are some caveats to these results; first, there is some carbon debris on the surface at locations (4) and (6) on the cathode, suggesting that the differences shown at these locations may be excessive. However, after close examination of all other images, there are no other trivial explanations for the large difference in peak magnitude between the anode and cathode sides. Even

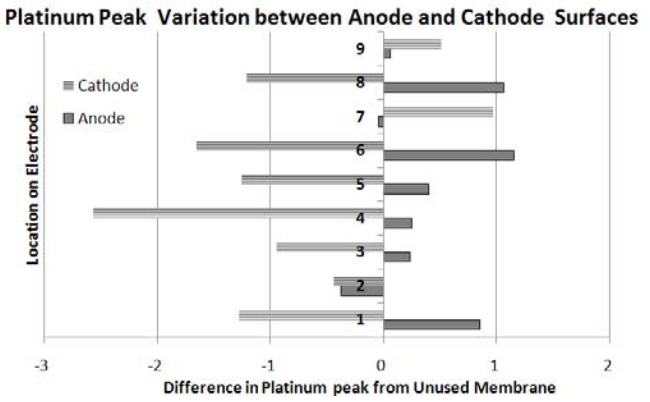

Figure 8. Platinum Peak Variation between Anode and Cathode Membrane Surfaces: Difference in relative magnitude of platinum peak in membrane used in Vertical Configuration I from that in an unused membrane

if the spraying process covered one side more effectively than the other, the ratios between the platinum and carbon peaks would not differ so drastically, since the carbon is applied along with platinum during this process. Therefore, if we accept that this difference is real, it appears that platinum is clustering on the anode side, or that platinum is being lost on the cathode side. As stated earlier, we have seen no evidence of clustering from the EDX/SEM maps. Nevertheless, a subtle leeching effect may be more difficult to detect visually. In terms of effects from flooding, there is considerably more platinum on the cathode in locations (7) and (9) than in any other region. Since these two locations are the most likely to be affected by any water accumulation, it is possible that oxidation of the carbon electrode[20] occurred at these locations via the mechanism described by equation (3.3) and led to an increase in platinum levels when compared to carbon.

For comparison, let us examine some higher magnification SEM micrographs of regions that show characteristic behaviors seen from fuel cell use. We have noted earlier that there are some clear differences between the Pt/C coverage on the sprayed membrane and that of the prefabricated GDL (Figure 5). Although the intended platinum per unit area should be the same, the spraying mechanism creates some irregularities on the surface (Figure 5B). However, when mapped using EDX, both types had the same elemental composition, regardless of morphology (Figures 5C, D).

Macroscopic differences that can be seen after use in fuel cell include cracking of the airbrushed surface; similar to the behavior seen with Nafion impregnation in (Figure 3) and residue from water droplets. We see surface cracking where flakes of Pt/C have come loose from the

Nafion surface (Figure 9A, B). When these are mapped using EDX, these show stronger sulfur and fluorine peaks, indicating portions of the top platinum layer has been removed. Images of water droplet residues were seen on the surface (Figure 9C, D). From Figure 9D it appears that the surface morphology has contributed to the pooling of these droplets. It is noted that the surface structure of the membrane undergoes swelling and other changes during the operation of the fuel cell, possibly contributing to this cracking behavior as no cracking was seen in the unused membrane (Figure 5B).

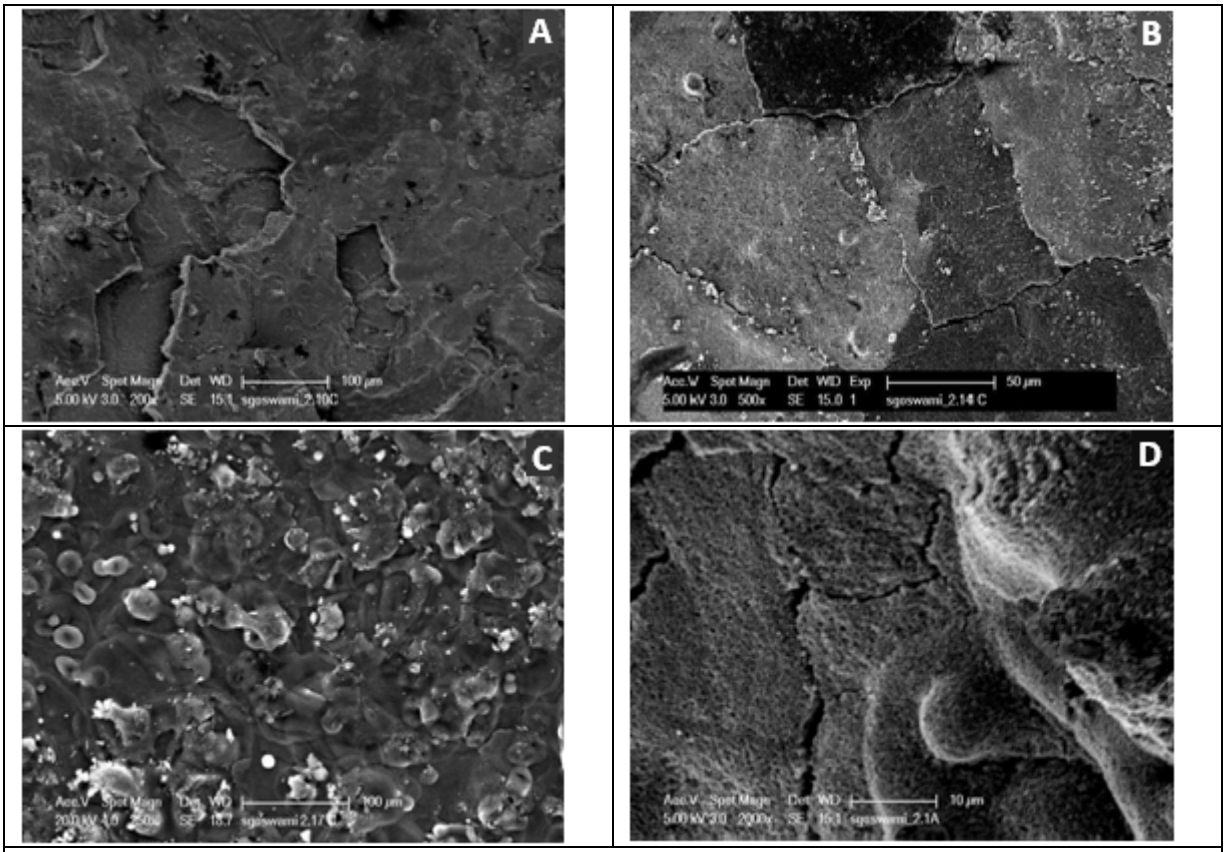

Figure 9. Common Degradation Effects on Airbrushed Membranes: **A** and **B** show effects of cracking on the membrane surface in locations (1) and (5), respectively; **C** and **D** show water droplet residues on membrane surface in locations (9) and (1), respectively.

Stoichiometric flow rates, regular current distribution, run for 100 hours

One of the difficulties in studying degradation mechanisms are the long time scales required. In other fields, time-temperature superposition allows for "long-term behavior" to be viewed on

shorter time frames, but higher temperatures can cause alternative degradation pathways in fuel cells[11]. For these reasons, we examined the most common orientation on a longer time scale.

Here we see the anode and cathode behavior over 100 hours of operation (Figure 10A, B). Although the initial current values are relatively close together, the cathode currents vary significantly during this time period. From previous work done by this lab, it is known that in most cases, the current in the fuel cell only drops when liquid water accumulates in the cathode gas flow channel and inhibits oxygen transport into the GDL[7]. Furthermore, the clear differences between the current-voltage curve for the anode and the cathode suggest flooding behavior (Figure 10C, D).

Low current readings as shown by these graphs signal flooding. The current value of the cathode at location (9) is lower than at location (5), which has been the lowest current in this orientation in non-flooding circumstances. The gradual decrease in current seen at the cathode (Figure 10B) suggests that the flooding occurred over time, and did not affect the cell behavior significantly until later. However, after the IV curve was obtained at 280,000 s or close to 80 hours, a steep increase in current was recorded. One explanation is that taking the IV curve allowed a long enough lapse in water production in the fuel cell to enable this electrode to recover contact with the reactant gases and thus recover current production.

To better see the effects of flooding on the main characteristics of the system, we examine the time-averaged current graphs from before (Figure 10E) and after (Figure 10F) flooding took place (but before recovery) It is clear immediately that flooding has affected locations (6) – (9), whereas the other locations have stayed mostly the same. Furthermore, in comparison to the time averaged graph in Figure 6D, the magnitude of differences between anode and cathodes current at all locations is higher for this case. This indicates that lower currents at one location from flooding may have driven lateral currents in other locations, exacerbating differences between the anode and cathode.

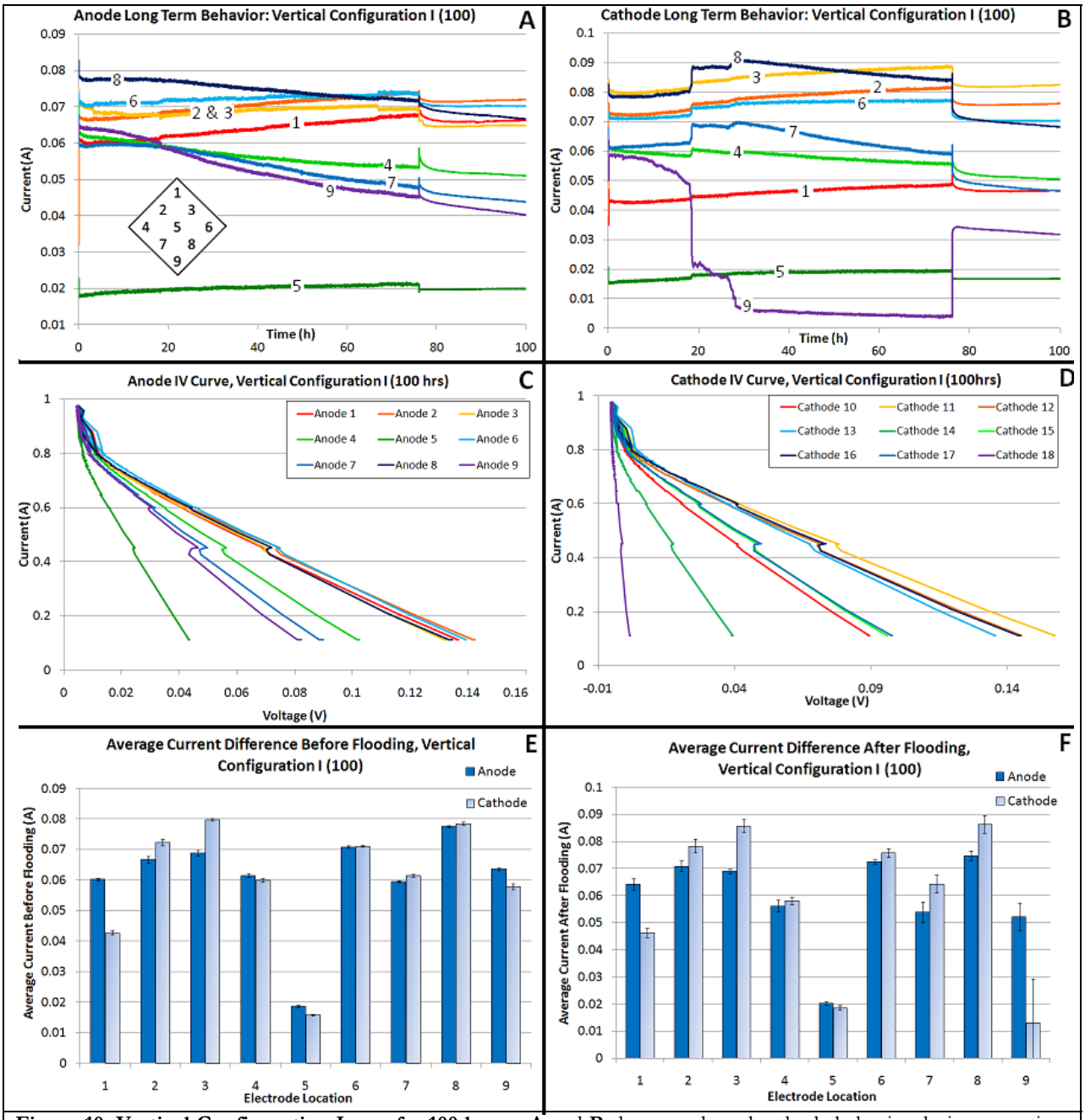

Figure 10: Vertical Configuration I, run for 100 hours: **A** and **B** show anode and cathode behavior during operation, **C** and **D** show IV curves at 78 hours for both anode and cathode. Cathode IV curve shows flooding at location (9). **E** shows time averaged currents before flooding, and **F** shows time averaged currents during flooding.

Although the fuel cell operated with almost identical starting positions in both the 50 hour and the 100 hour case, the actual current profiles during operation varied considerably. The average current for each run differed very little, from 56 mA to 58 mA. However, the flooding behavior seen in the second situation was most probably from the cell at a slight angle.

Possible corrosive conditions obtained from effective voltage calculation at 9 C

As described earlier, compositional differences across the fuel cell flow region create local potential differences and changes in local internal resistance that yield local current differences. Since there does not appear to be flooding at the anode interface, there is no hydrogen starvation seen in this cell. The situation at the cathode is shown schematically in Figure 11A, where 9 C is starved for oxygen, but the adjacent location (7) has the necessary reactant. Both 7 C and 9 C have the same overall potential difference, potentially leading to the oxidation of the carbon electrode by water by reaction (3.3).

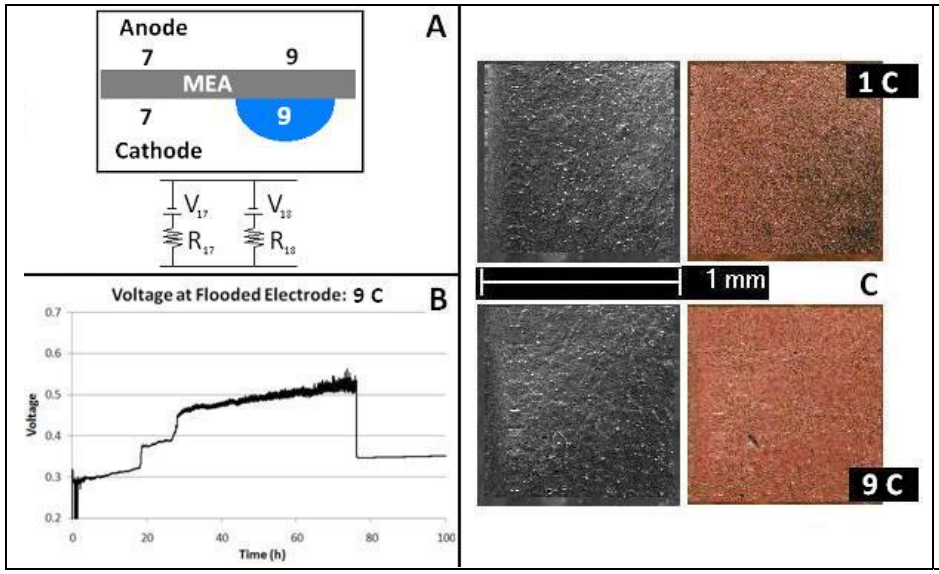

Figure 11. Description of Flooded Electrode 9 C: **A** Equivalent circuit representation showing the effect of liquid in the flow region causing local starvation at the membrane electrode interface. **B** Effective voltage increases during flooding behavior. **C** Comparison of flooded and not-flooded electrodes at the cathode; left image is SEM at 20 kV beam acceleration, 50 X, right image is EDX map, carbon (red), fluorine (yellow), sulfur (purple) and platinum (orange) overlayed on SEM image

Partial pressures of reactant gases in the flow region were calculated assuming 80% H_2 fuel conversion into water and a total pressure of 1.2 bar inside the fuel cell. Since only electrode 9 C showed flooding behavior and even 9 A continued to function throughout operation, a new cathode mass transfer coefficient was calculated assuming that 1/18 of the GDL volume was filled with liquid water. Using equation (3.8), the new k_c is found to be 1.03×10^{-8} mol/m^2-s-Pa. Equations (3.9) and (3.10) were applied to calculate the partial pressures at the electrode-electrolyte interface using a GDL area of 1.008×10^{-3} m^2. Finally, the effective voltage at 9 C was calculated using equation (3.11) assuming a battery voltage of 0.5 V and a water activity of 1 from the presence of

liquid water, yielding the voltage profile shown in Figure 11B. From this profile, it is evident that the effective voltage during flooding is much higher than in the non-flooded case. Many of these values are in the range of voltages found from corrosion conditions during start-up or during the movement of a drying front[19, 22]. Nevertheless, even though most of these values are higher than the potential required to oxidize the carbon electrode as per reaction (3.3), the fact that flooding was not sustained may affect the level of corrosion on the electrode surface.

For this reason, we examined the electrode surface at location (1) and location (9) on the cathode to see the difference from flooding. The SEM/EDX images for the cathode at 1 C and 9 C are shown in Figure 11C. From this map, it seems that 9 C is more uniform in color; however both SEM images look very similar. Using the same strategy as with the 50 hour case described earlier, the platinum peak magnitude was normalized to the carbon peak for both locations The results were quite striking, since the ratio of platinum and carbon peaks for 1 C was nearly three-fold the ratio for 9 C (spectra shown in Appendix D). This suggests that either the platinum in 9 C has been depleted or that the surface morphology has changed. For these images, the regions mapped were specifically chosen that showed little flaking at the surface and had no carbon debris visible. Therefore, it is likely that this elemental composition difference is as a result of flooding at 9 C.

The effective loss of this electrode from the system was < 2% of the total current, similar to results seen in previous experiments where the electrode segment was actually disconnected from the electrode (unpublished data, JBB). The loss of this electrode was mitigated by current increases at locations (1), (2), (3) and (6) on the cathode, all of which incurred a current increase of 10% after the onset of flooding.

Stoichiometric flow rates, aberrant current distribution, failed at 17 hours

In most fuel cells, the flow field is not well controlled over the entire area of the fuel cell. In fact, current distribution is usually not visible without a segmented electrode; therefore unusual

current distributions are not recorded. As a result, there are often pockets where there is better mixing and other subtle factors which lead to variable current densities. In the extreme situation, most of the current would be concentrated in a single region rather than evenly distributed over the entire MEA.

A version of this extreme case is explored with the self-draining orientation. In Figure 12, we see the behavior of the anode and the cathode in a cell in the self-draining position where the currents are unevenly distributed. This current disparity occurs when different pillars are screwed in varying amounts, causing some of them to have substantially better contacts with the MEA surface. As a result, the maximum current is much higher (130 mA rather than 75 mA). This led to a 36 mA standard deviation among all eighteen currents, in contrast to the 15 mA standard deviation seen in previous iterations.

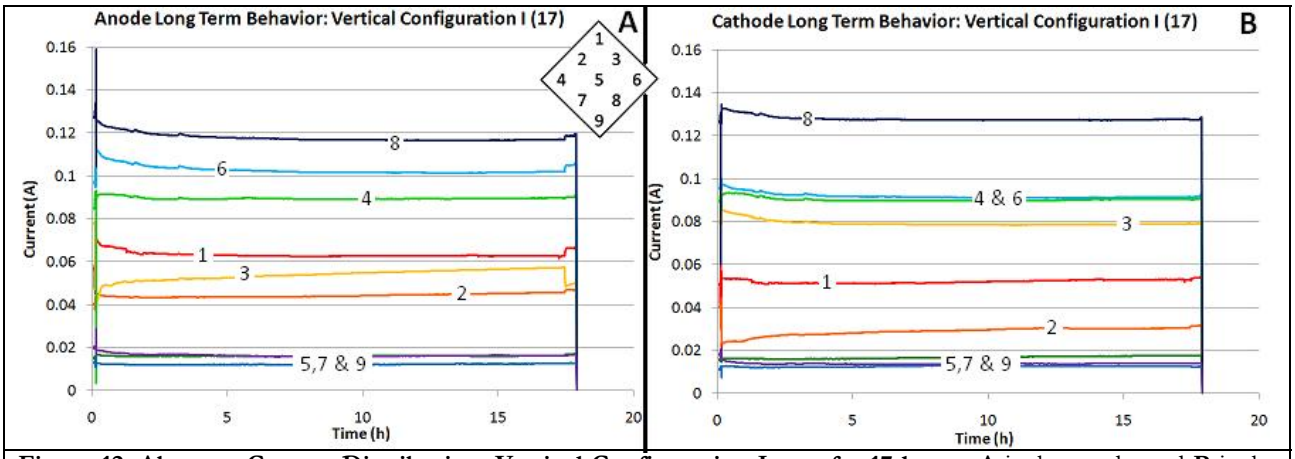

Figure 12. Aberrant Current Distribution, Vertical Configuration I, run for 17 hours: **A** is the anode, and **B** is the cathode current distribution throughout operation. The sharp drop at 17 hours indicates membrane failure. Total voltage dropped to 0.45 V from 0.5 V, total current was maintained at 1.0 A.

However, what is most unusual is the region of the membrane that failed during operation. From the data shown in Figure 12, it seems that the region that is hottest and most likely to fail from degradation[11] would be area (8). The region that failed was the membrane surrounding area (1); even though currents in surrounding regions were in the typical range for both anode and cathode. When IV curves were completed for this orientation, no flooding behavior was seen (data not shown).

To determine the cause of this extreme corrosion, we compared the inside GDL surface (the side touching the membrane) at 1 C, the region where the membrane failed, from both the failed MEA (Figure 13A) and from a functional MEA in the same orientation (Figure 13B). The material used for the GDL/MPL is identical to that shown earlier, except that there is no catalyst layer on the MPL surface. The functional GDL (Figure 13B) showed regular cracking similar to that resulting from Nafion impregnation (Figure 3D), ostensibly from wetting on the surface and subsequent drying, thus cracking the MPL. In contrast, the frequency of cracking is much higher in the failed MEA (Figure 13A).

One hypothesis for this corrosion is reactant crossover from defects in the membrane. If these defects were present when testing began, no current would have been produced in the cell at all. Therefore, we conclude that failure of the membrane was wrought by the aberrant current distribution conditions (Figure 12). As a result of failure, hydrogen and oxygen reacted in a combustion reaction at the membrane-electrode interface, exacerbating these corrosion effects. Since corrosion was not immediately detected, the inlet gas flows were not stopped, thus continuing the degradation process. Furthermore, the combustion reaction was catalyzed by the platinum present on the membrane. The resulting failed membrane appeared as seen in Figure 13C. This is compared to the case where the defect in the membrane was detected immediately after failure (Figure 13D). In the latter case, it appears that the defect is manifested via thinning of the membrane in the failure region, as evidenced by the shiny surface seen in location (1). In contrast, membrane that failed after 17 hours (Figure 13C) has already degraded completely in location (1) and this degradation mechanism has begun to affect other regions.

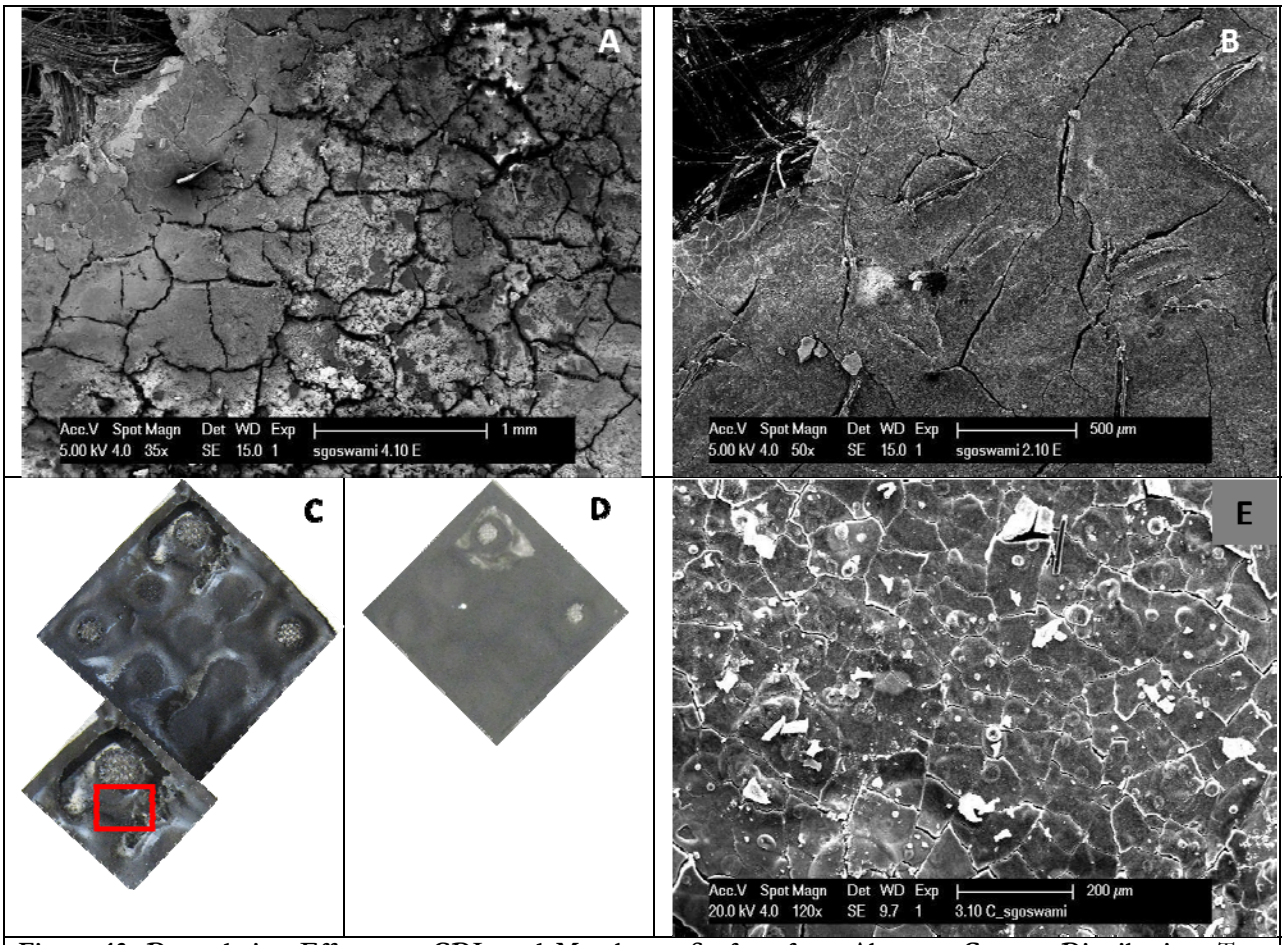

Figure 13. Degradation Effects on GDL and Membrane Surface from Aberrant Current Distribution: Two electrodes imaged at location (1) on the cathode side, used in two different fuel cells that were used in Vertical Configuration I. **A** shows the GDL from an MEA that failed after 17 hours of operation, and **B** shows the GDL from an MEA that was functional throughout 50 hours of operation. **C** shows the damaged membrane (all 9 locations on the cathode) from the same MEA that failed after 17 hours. **D** shows a damaged membrane (all 9 locations on the cathode) from an MEA that failed after 5 minutes and was immediately removed. **E** is the extent of damage from membrane in SEM, image taken at location shown in red box in **C**.

In both cases, we saw that the initial membrane defect and the subsequent crossover event occurred at location (1). This may indicate that the inlet region is more susceptible to this mechanism of failure. To examine further effects from the combustion reaction, the region of the failed membrane selected in Figure 13C was imaged using an SEM (Figure 13E). In contrast to damage from flaking and water droplets seen in functional membranes (Figure 9), the cracking on the membrane surface in (Figure 13E) is more frequent and pronounced. One explanation for this behavior is the requirement of platinum to catalyze the combustion reaction. Since platinum is not found uniformly across the membrane, these reactions will be concentrated in locations where it is

present at the highest concentrations. EDX mapping was also used to examine any changes in elemental composition from this extreme degradation (map shown in Appendix E). From the map, it appears that the lighter regions on the SEM image are platinum particles. Since in other membranes, the platinum is more evenly distributed, this further supports our hypothesis. The low amount of platinum relative to carbon as calculated from the peak magnitudes implies that the platinum has been depleted relative to the carbon or that it is in clusters on the membrane surface.

5.3.2 Vertical Configuration II (VC-II); Gas Flow against Gravity
Stoichiometric flow rates, run for 35 hours[†]

In orientation VC-II, the current behavior and distribution has not significantly changed compared to the upright case. The total current and total voltage are still 1.0 A and 0.5 V, as was the case with VC-I and the long term current distributions at the anode and cathode are shown (Figure 14A, B). It appears that there has been some redistribution from the VC- I case as to which location provides the most favorable reaction conditions. However, it is not clear if this favorability is directly related with the orientation, since there does not seem to be a clear correlation between electrode location and current magnitude. In Figure 14C, it is clear that the anode and cathode currents match up well in this orientation. It is not yet apparent if the behavior of the fuel cell in this orientation matches the variation in current density profiles observed in previous experiments.[7] However, periodic oscillations were not seen in any of the distributed electrodes. This is not surprising, as the stirred tank nature of the channel-less fuel cell would lead to alternative current behaviors from the segmented anode fuel cell.

[†] The shortened run time in this case is from the supply of O_2 running out, rather than failure from the MEA or the fuel cell

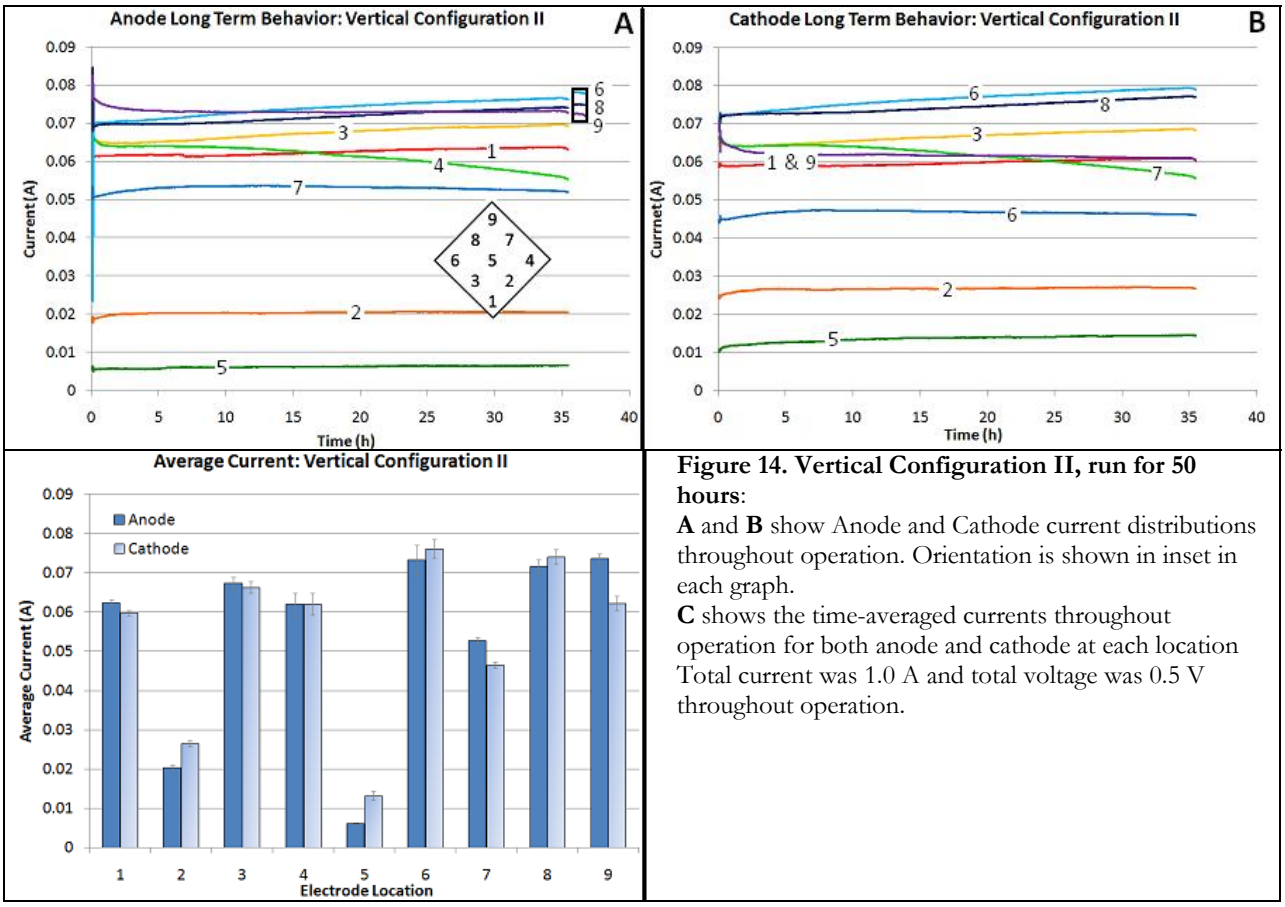

Figure 14. Vertical Configuration II, run for 50 hours:
A and **B** show Anode and Cathode current distributions throughout operation. Orientation is shown in inset in each graph.
C shows the time-averaged currents throughout operation for both anode and cathode at each location Total current was 1.0 A and total voltage was 0.5 V throughout operation.

5.3.3 Horizontal Configuration I (HC-I); Anode and Cathode Coplanar Stoichiometric flow rates, run for 50 hours

In this orientation, the currents were also fairly evenly distributed (Figure 15A, B). As expected, the total current and total voltage was the same as with other orientations, at 1.0 A and 0.5 V, respectively. An additional key similarity to VC-I was that small perturbations disturbed the anode current more significantly than the cathode current. The first disturbance in Figure 15A involved making a better contact at location (8) and thus cannot be regarded as a small perturbation, but a subsequent disturbance at 43 hours showed a much greater impact on the anode than the cathode. This further supports the idea that the favorable reaction regions on the cathode are less likely to change from the movement of condensed water.

Another remarkable feature of this particular orientation is that despite visual confirmation that there is some accumulation of water around the three bottommost locations (data not shown),

there does not seem to be any effects on the currents at these locations from this accumulation. Furthermore, in the present arrangement, it would have been necessary for the water to accumulate to the halfway point in order to exit the plenum. There are two explanations for this phenomenon. The first is that there was leakage from the edges of the fuel cell that enabled the water to exit. This appears to be at least partially responsible, as wet regions were found at the edge of the cell after use. Another explanation is that there was some oscillation in water production such that the cell was occasionally filled to the halfway point and at other times water production was lower. Mixing enables this water to humidify the incoming dry reactant streams and maintain current levels. Moreover, it is likely that this water is not flooding the entire bottom plenum region but is rather wicking on the surface of the polycarbonate plate.

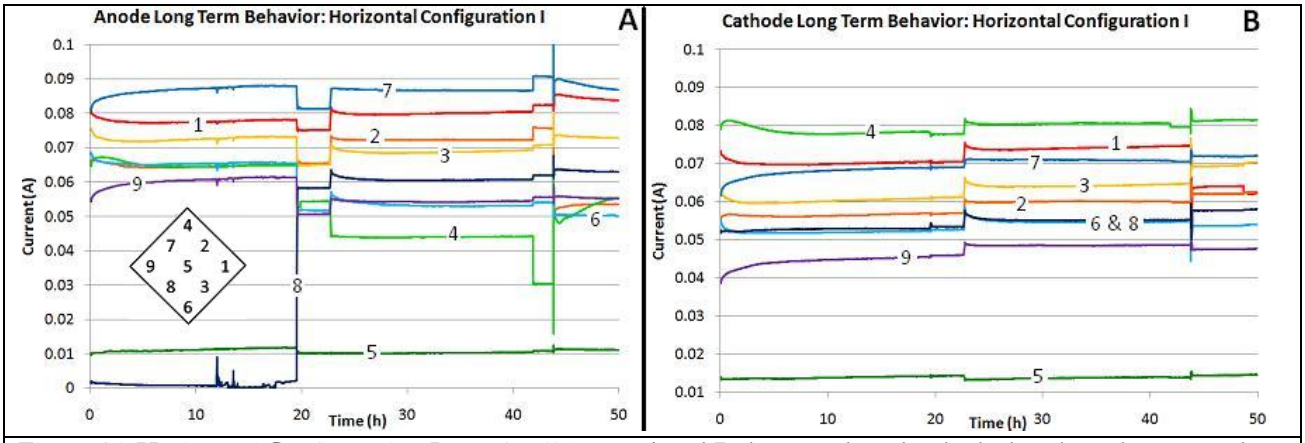

Figure 15. Horizontal Configuration I, run for 50 hours: **A** and **B** show anode and cathode data throughout operation, orientation is shown in inset for each graph.

5.3.4 Horizontal Configuration II (HC-II); Anode below Cathode Plane Stoichiometric flow rates, run for 50 hours

In this final orientation, we see some interesting behavior not seen in any of the other three orientations (Figure 16A, B), although the total voltage (0.5 V) and total current (1.0 A) was the same as with the other orientations. There was flooding seen in this case, as expected, although it appears that the cell was tilted toward locations (3), (6) and (8) such that these accumulated more water. However, only location (8) was flooded enough that no current was produced there. As seen

with VC-I (100) in (Figure 10), the flooded region and associated electrode is particularly sensitive to small perturbations. At the same time as there are extensive flooding effects seen at the anode, there is relatively little effect at the cathode, even at locations that are flooded. This suggests that the systems may start-up with similar characteristics, but once the fuel cell is running, the effects at one side have little influence on the other.

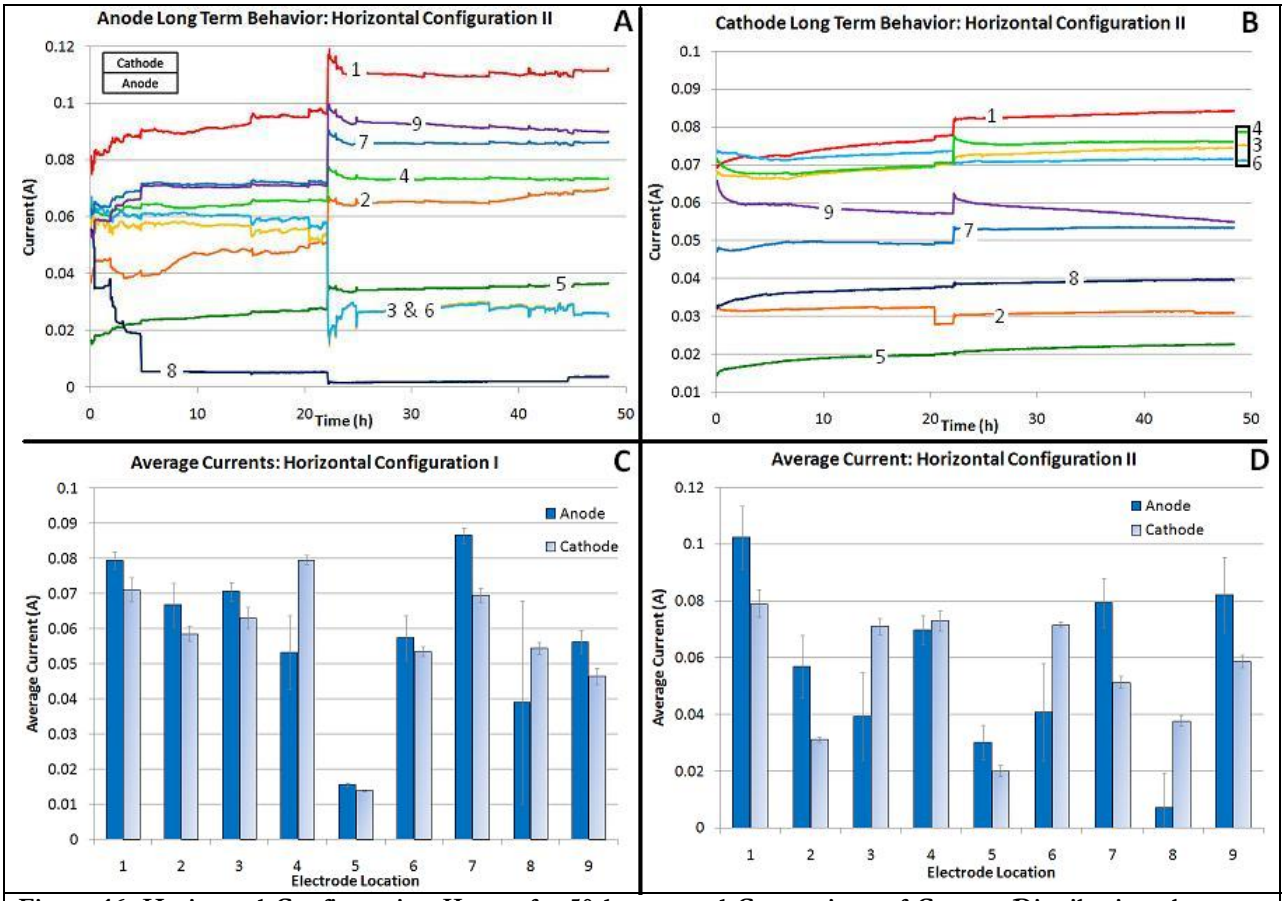

Figure 16. Horizontal Configuration II, run for 50 hours, and Comparison of Current Distributions between two Horizontal Orientations: **A** and **B** show current distributions throughout operation at the anode and cathode, respectively. Orientations are shown in inset for each graph. **C** shows time averaged current at both anode and cathode for all locations during HC-I. **D** shows the same data for HC-II.

Effective voltages at the flooded electrodes were calculated in the same fashion as for 9 C in VC-I (100). From this analysis, maximum voltages of 0.46 V at location (8), 0.38 V at locations (3) and (6) were obtained (graphs over time shown in Appendix F). These values are much lower than the maximum voltage calculated for 9 C of 0.57 V. This suggests that despite the visible flooding

effects, it was not as severe as in the previous case. The shorter time frame may also be a factor, as we saw that severe flooding effects were time delayed in the previous case. Lower effective resistances from water blocking the electrodes from reactants could also result in lower effective voltages.

Finally, we examined the effects that this widespread flooding has had on the anode-cathode current difference. In Figure 16C we see the time-averaged currents at each location for HC-I and in Figure 16D we see the data for HC-II. In contrast to the vertical orientations examined earlier, the magnitude of the difference in anode and cathode currents at the same location was higher, particularly for HC-II. Furthermore, it appears that in order to mitigate the flooding effects on one side of the MEA, the obverse current is increased. Another explanation is that the position of the anode in the flooding position actually increased the currents until there was excessive accumulation, and as a result, the reactants were exceptionally well-humidified.

6. Conclusions

From this analysis of various orientations and current distributions in the self-draining channel-less fuel cell, it is clear that particular conditions are more likely to lead to degradation than others. In addition, inherent characteristics of the MEA with respect to anode and cathode behavior were also discovered. Firstly, results from all four orientations suggested that cathode currents and current distributions derive from inherent reaction and flow field conditions, whereas their anode counterparts are more easily influenced by transient conditions such as condensation. This was supported by the stability of the cathode current distributions throughout operation, except in cases where flooding was observed. These reaction "hot-spots" may be more susceptible to degradation on longer time scales, although no difference in surface morphology and elemental composition was observed in this study.

Secondly, flooding appears to have a subtle, but significant degradation effect on this time scale. When flooding was seen in Vertical Configuration I, the effective voltage in the flooded location increased by 0.2 V as a result of increased resistance in this region. When the flooded and non-flooded regions of the electrode were examined using SEM and EDX, it appeared that platinum was depleted in the flooded region. The differences between anode and cathode currents at the same locations for the flooded case suggests that lateral currents were responsible for redistributing current to the remainder of the electrode when location (9) was flooded. Flooding itself resulted in <2% loss in total current. It also appeared that the effects of flooding operation on cell performance were time delayed.

A more striking degradation effect was seen from aberrant current distributions. Although the degradation from combustion of hydrogen at the cathode was exacerbated by the presence of platinum on the membrane surface, the initial defect was most probably a function of the irregular current distribution among the nine regions. However, the initial failure location was close to the inlet, rather than at the locations with the highest currents. In subsequent trials, failure continued to occur most frequently at the inlet region. Since the inlet is the driest part of the membrane, it may be more susceptible to this failure mechanism.

In SEM and EDX images of the failed inlet region of the MEA, cracking behavior was much more prominent than in other cases. The cracks on the membrane appeared to follow the locations where platinum was found, further supporting the idea that platinum aggravates the combustion reaction[11] once crossover begins to occur. Since platinum is not found uniformly across the membrane, the cracks occur where it is most abundant.

For Vertical Configuration II, the same total current (1.0 A) and total voltage (0.5 V) was found as with VC-I. The current distributions remained constant throughout operation. The type of variation in the form of random fluctuations was not seen[7], but the orientation was only tested once.

For the two horizontal configurations, it appeared that the alternative orientation led to enhanced mixing for auto-humidification. This was seen most prominently with Horizontal Configuration II, where those anode locations that were not flooded showed exceptionally high currents.

As fuel cells are implemented into vehicle and remote systems, it is key that degradation is well controlled and minimized. The fuel cell systems used by Toyota are identical to the self-draining cell studied in this thesis. If a single pillar or equivalent is disconnected during operation, the resulting aberrant current profile could lead to rapid failure of the fuel cell system. In the same vein, particular orientations increase the occurrence of flooding using this design. If flooding does increase degradation rate, improved water removal systems may need to be designed.

7. Future Experimentation

Some degradation phenomena can only be seen after many hundreds of hours of testing. In the absence of this time, the maximum time that any of these orientations was run was only four days. Many of the above effects may be more clearly identified with longer experiments. Furthermore, many factors were tested only in the self-draining case. Alternative conditions that lead to flooding could be tested in the other three orientations as well. Secondly, for these suggested long-term studies, the design of the fuel cell should be changed subtly. The pillars of the cell should be structured such that all locations obtain equal contact with the MEA in the closed cell. After these experiments are run with equally distributed pillars, they should be repeated with specifically altered irregular current distributions. This can determine if the degradation from aberrant current profiles seen in this thesis is observed in both high and low current locations.

8. References

1. Barbir, F., *PEM fuel cells : theory and practice*. Elsevier Academic Press: Amsterdam ; Boston, 2005.
2. Gasteiger, H. A.; Gu, W.; Litteer, B.; Makharia, R.; Brady, B.; Budinski, M.; Thompson, E.; Wagner, F. T.; S.G., Y.; Yu, P. T., Catalyst Degradation Mechanisms in PEM and Direct Methanol Fuel Cells. In *Mini-micro fuel cells : fundamentals and applications*, Kakaç, S.; Pramuanjaroenkij, A.; Vasiliev, L., Eds. Springer: Dordrecht ; London, 2008; pp 225-233.
3. Hogarth, W. H. J.; Benziger, J. B., Dynamics of autohumidifed PEM fuel cell operation. *Journal of the Electrochemical Society* **2006,** *153* (11), A2139-A2146.
4. Siegel, J. B.; Mckay, D. A.; Stefanopoulou, A. G.; Hussey, D. S.; Jacobson, D. L., Measurement of liquid water accumulation in a PEMFC with dead-ended anode. *Journal of the Electrochemical Society* **2008,** *155* (11), B1168-B1178.
5. Benziger, J.; Chia, J. E.; Kimball, E.; Kevrekidis, I. G., Reaction dynamics in a parallel flow channel PEM fuel cell. *Journal of the Electrochemical Society* **2007,** *154* (8), B835-B844.
6. Benziger, J. B.; Hogarth, W. H. J.; Woo, C., Operation of Polymer Electrolyte Membrane Fuel Cells with Dry Feeds. *Electrochemical Society Transactions* **2007,** *12* (1), 165-176.
7. Kimball, E.; Whitaker, T.; Kevrekidis, Y. G.; Benziger, J. B., Drops, slugs, and flooding in polymer electrolyte membrane fuel cells. *Aiche Journal* **2008,** *54* (5), 1313-1332.
8. Zhang, J.; Zhang, J., Catalyst Layer/MEA Performance Evaluation. In *PEM fuel cell electrocatalysts and catalyst layers : fundamentals and applications*, Zhang, J., Ed. Springer: London, 2008; pp 965-1002.
9. Chia, E. S. J.; Benziger, J. B.; Kevrekidis, L. G., STR-PEM fuel cell as a reactor building block. *Aiche Journal* **2006,** *52* (11), 3902-3910.
10. Carrette, L.; Friedrich, K. A.; Stimming, U., Fuel cells: Principles, types, fuels, and applications. *Chemphyschem* **2000,** *1* (4), 162-193.
11. Stevens, D. A.; Dahn, J. R., Thermal degradation of the support in carbon-supported platinum electrocatalysts for PEM fuel cells. *Carbon* **2005,** *43* (1), 179-188.
12. de Bruijn, F. A.; Dam, V. A. T.; Janssen, G. J. M., Durability and degradation issues of PEM fuel cell components. *Fuel Cells* **2008,** *8* (1), 3-22.
13. Howard, E. The Design of Optimal Material Combinations for the Membrane Electrode Assembly of a Proton Exchange Membrane Fuel Cell. Senior, Princeton University, Princeton, 2006.
14. Zhang, H.; Wang, X.; Zhang, J.; Zhang, J., Conventional Catalyst Ink, Catalyst Layer, and MEA Preparation. In *PEM fuel cell electrocatalysts and catalyst layers : fundamentals and applications*, Zhang, J., Ed. Springer: London, 2008; pp 889-916.
15. Lee, S. J.; Mukerjee, S.; McBreen, J.; Rho, Y. W.; Kho, Y. T.; Lee, T. H., Effects of Nafion impregnation on performances of PEMFC electrodes. *Electrochimica Acta* **1998,** *43* (24), 3693-3701.
16. Weber, A. Z.; Newman, J., Effects of microporous layers in polymer electrolyte fuel cells. *Journal of the Electrochemical Society* **2005,** *152* (4), A677-A688.
17. Yu, X. W.; Ye, S. Y., Recent advances in activity and durability enhancement of Pt/C catalytic cathode in PEMFC - Part I. Physico-chemical and electronic interaction between Pt and carbon support, and activity enhancement of Pt/C catalyst. *Journal of Power Sources* **2007,** *172* (1), 133-144.
18. Shen, P. K., PEM Fuel Cell Catalyst Layers and MEAs. In *PEM fuel cell electrocatalysts and catalyst layers : fundamentals and applications*, Zhang, J., Ed. Springer: London, 2008; pp 355-380.
19. Reiser, C. A.; Bregoli, L.; Patterson, T. W.; Yi, J. S.; Yang, J. D. L.; Perry, M. L.; Jarvi, T. D., A reverse-current decay mechanism for fuel cells. *Electrochemical and Solid State Letters* **2005,** *8* (6), A273-A276.
20. Kinoshita, K., *Carbon : electrochemical and physicochemical properties*. Wiley: New York, 1988.

21. Tang, H.; Qi, Z. G.; Ramani, M.; Elter, J. F., PEM fuel cell cathode carbon corrosion due to the formation of air/fuel boundary at the anode. *Journal of Power Sources* **2006,** *158* (2), 1306-1312.
22. Roen, L. M.; Paik, C. H.; Jarvic, T. D., Electrocatalytic corrosion of carbon support in PEMFC cathodes. *Electrochemical and Solid State Letters* **2004,** *7* (1), A19-A22.
23. Stevens, D. A.; Hicks, M. T.; Haugen, G. M.; Dahn, J. R., Ex situ and in situ stability studies of PEMFC catalysts. *Journal of the Electrochemical Society* **2005,** *152* (12), A2309-A2315.
24. Umeda, M.; Maruta, T.; Inoue, M.; Nakazawa, A., Cathode Platinum Degradation in Membrane Electrode Assembly Studied Using a Solid-State Electrochemical Cell. *Journal of Physical Chemistry C* **2008,** *112* (46), 18098-18103.
25. Tada, T., High Dispersion Catalysts including Novel Carbon Supports. In *Handbook of fuel cells : fundamentals, technology, and applications*, Vielstich, W.; Lamm, A.; Gasteiger, H. A., Eds. Wiley: Chichester, England ; Hoboken, N.J., 2003; Vol. 3, pp 481-488.
26. Darling, R. M.; Meyers, J. P., Kinetic model of platinum dissolution in PEMFCs. *Journal of the Electrochemical Society* **2003,** *150* (11), A1523-A1527.
27. Willsau, J.; Heitbaum, J., The Influence of Pt-Activation on the Corrosion of Carbon in Gas-Diffusion Electrodes - a Dems Study. *Journal of Electroanalytical Chemistry* **1984,** *161* (1), 93-101.
28. Schulze, M.; Wagner, N.; Kaz, T.; Friedrich, K. A., Combined electrochemical and surface analysis investigation of degradation processes in polymer electrolyte membrane fuel cells. *Electrochimica Acta* **2007,** *52* (6), 2328-2336.
29. Song, J. M.; Cha, S. Y.; Lee, W. M., Optimal composition of polymer electrolyte fuel cell electrodes determined by the AC impedance method. *Journal of Power Sources* **2001,** *94* (1), 78-84.
30. Russ, J. C., *Fundamentals of energy dispersive x-ray analysis*. Butterworths: London ; Boston, 1984.
31. Lee, S.; Younan, H.; Siping, Z.; Zhiqiang, M. In *Studies on Electron Penetration Versus Beam Acceleration Voltage in Energy Dispersive X-Ray Microanalysis*, International Conference on Software Engineering, Kuala Lumpur, Malaysia, IEEE Explore: Kuala Lumpur, Malaysia, 2006.

Appendix A: Thickness of Each Component in Membrane-Electrode Assembly

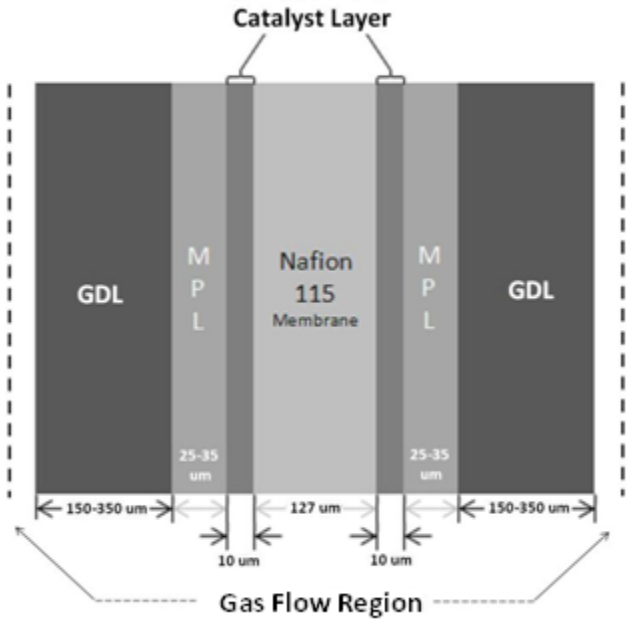

MEA Schematic, measurements adapted from de Bruijn et al. These measurements are assumed using a 0.005" Nafion membrane

From this it is easy to see which layers are thickest and those that are most prone to losses from degradation. We can also compare these thicknesses with the values for the catalyst layer-MPL structure measured using the SEM in Figure 4.

Appendix B: Element Maps for Anode Image Overlays in Figure 7

All of the oxygen spectral maps resemble the following image: 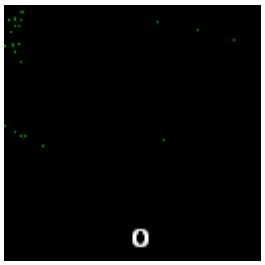

As a result, they will not be included in the interest of space.

1A: 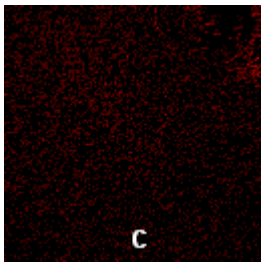

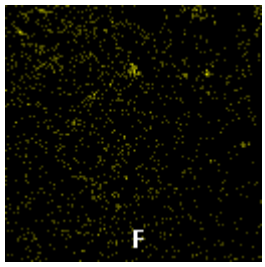

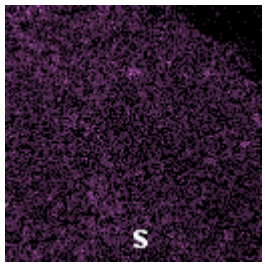

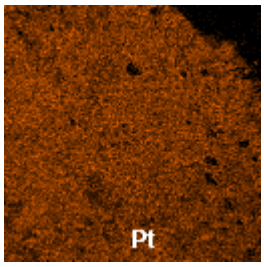

2A: 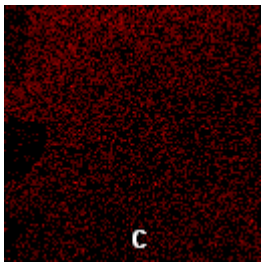

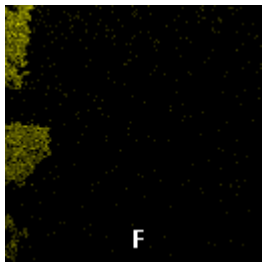

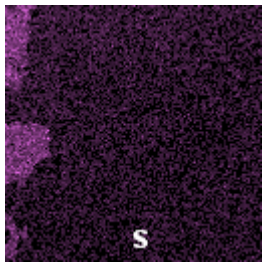

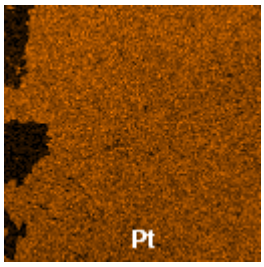

3A: 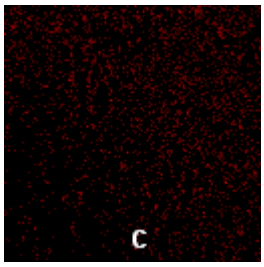

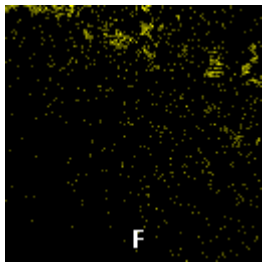

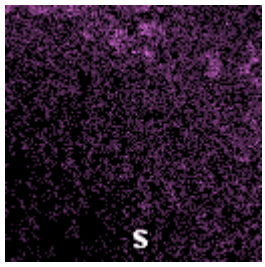

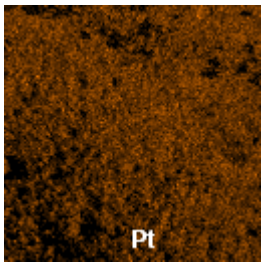

4A: 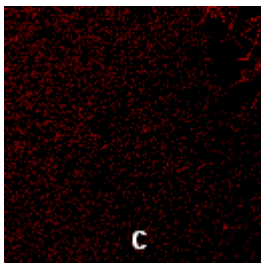

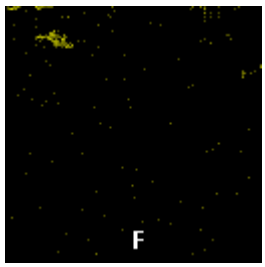

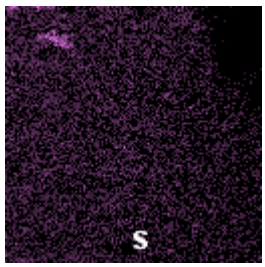

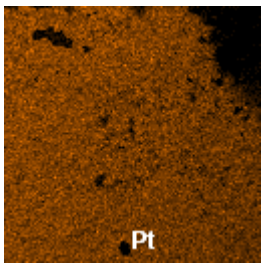

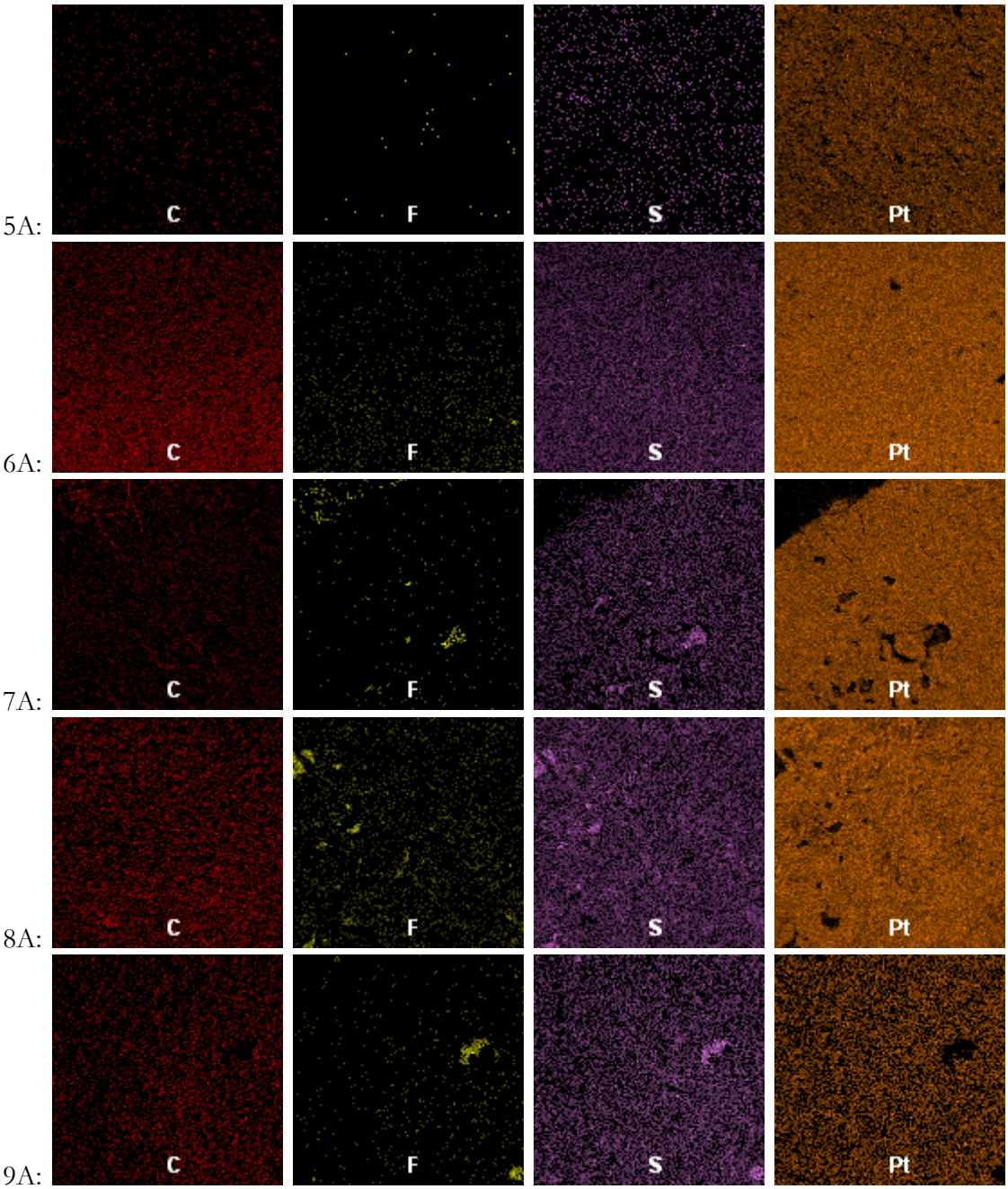

Even from these more detailed elemental maps, it is evident that any degradation mechanism was uniform across all locations on the anode.

Appendix C: Cathode SEM/EDX Profiles for Vertical Configuration I (50)

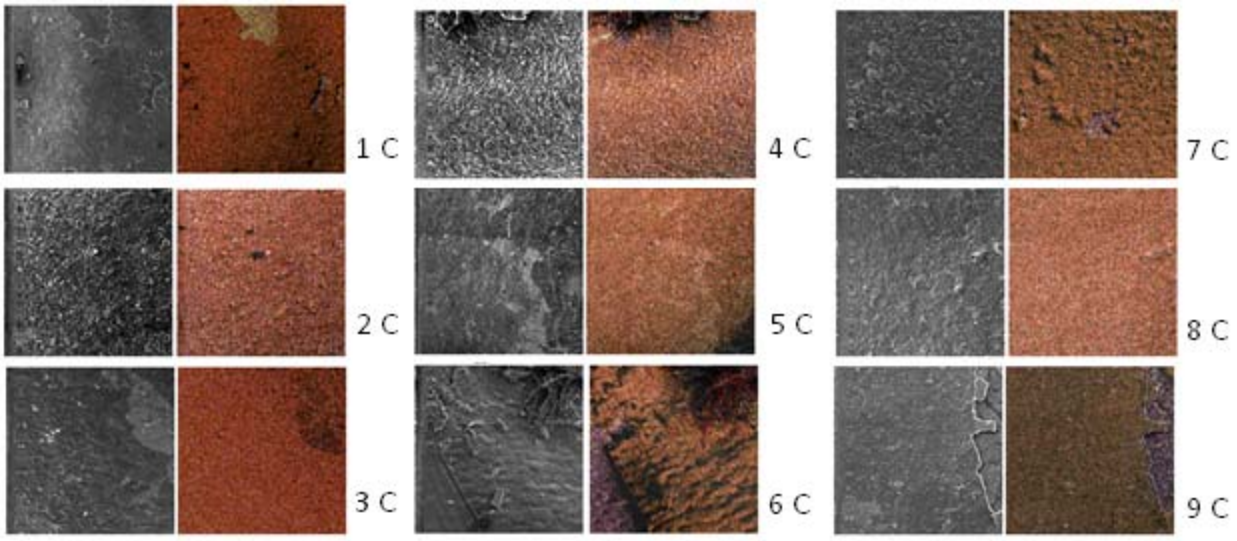

Note: 6 C was taken in an unusual location and at slightly higher magnification, thus leading to an image that does not resemble the other locations. This is merely an artifact of the process used to select electrode regions for magnification.

As we can see from these maps, the degradation across the cathode was also uniform in this configuration.

Appendix D: 1 C and 9 C EDX Spectra for Vertical Configuration I (100)

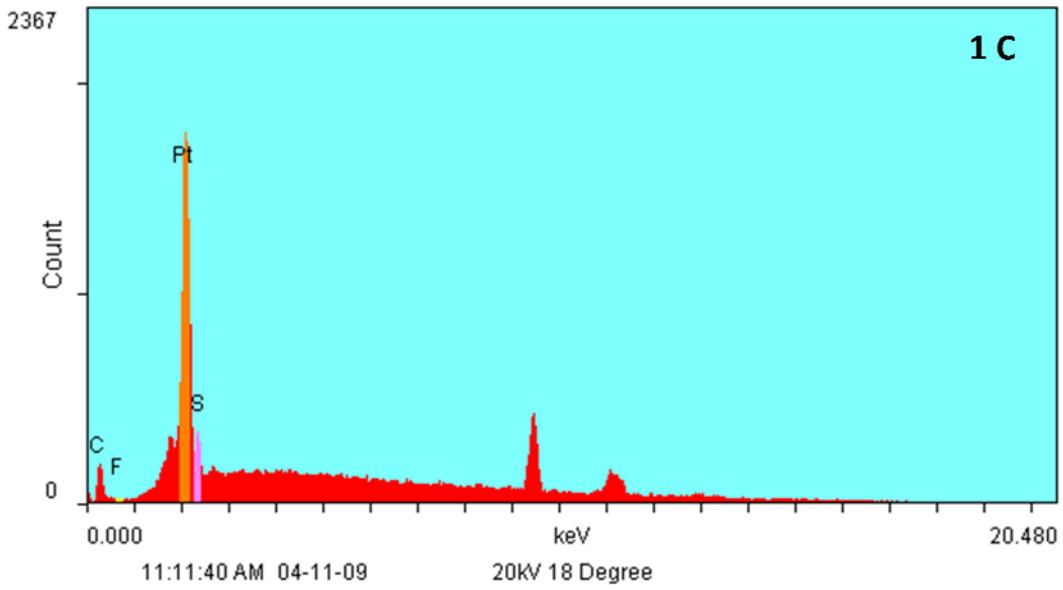

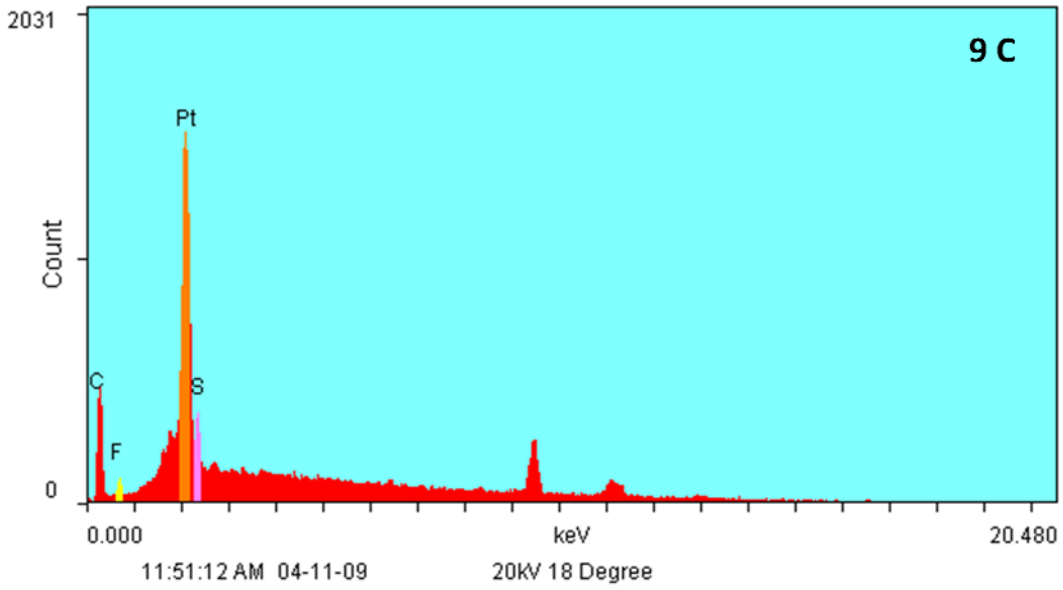

Although the absolute magnitudes of each peak can vary from sample to sample, relative amounts of each element can be compared using ratios. For this case, the ratio of Pt: C in 1 C is approximately 7.5 and the ratio of Pt: C in 9 C is 3.2.

Appendix E: Elemental Composition for 1 C in Vertical Configuration I (17)

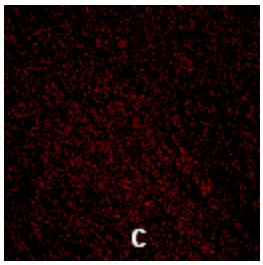

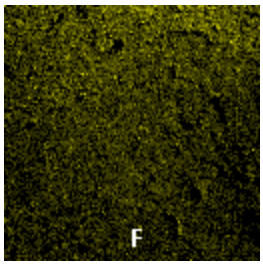

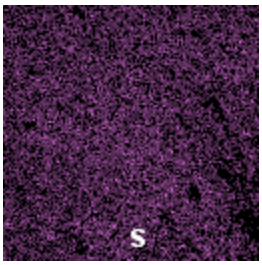

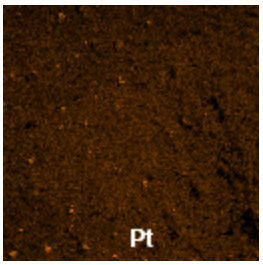

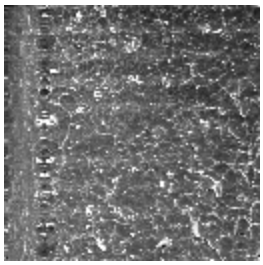
(SEM Image at 50X, 20 kV beam voltage)

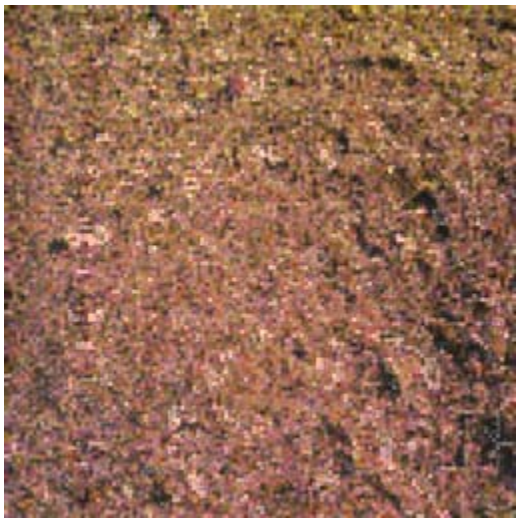
Above elemental maps overlayed on SEM image

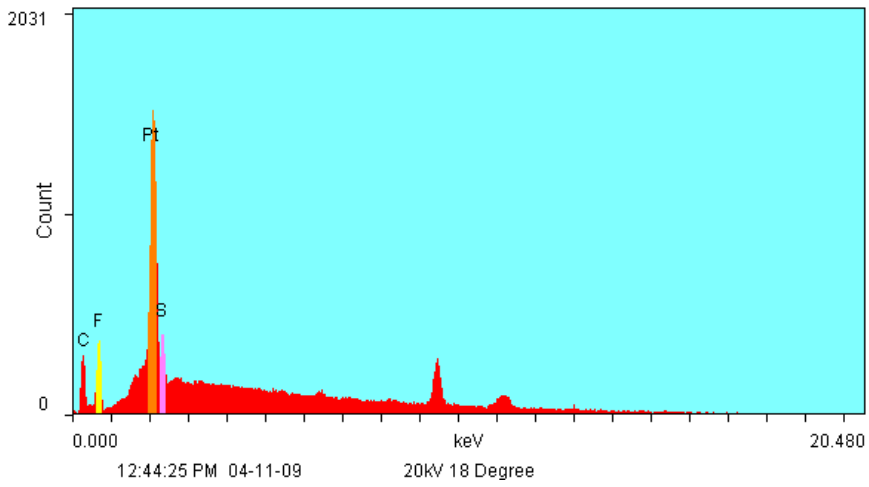

Spectrum for EDX mapping

Appendix F: Effective Voltages at 3 A, 6 A and 8 A from Flooding in Horizontal Configuration II

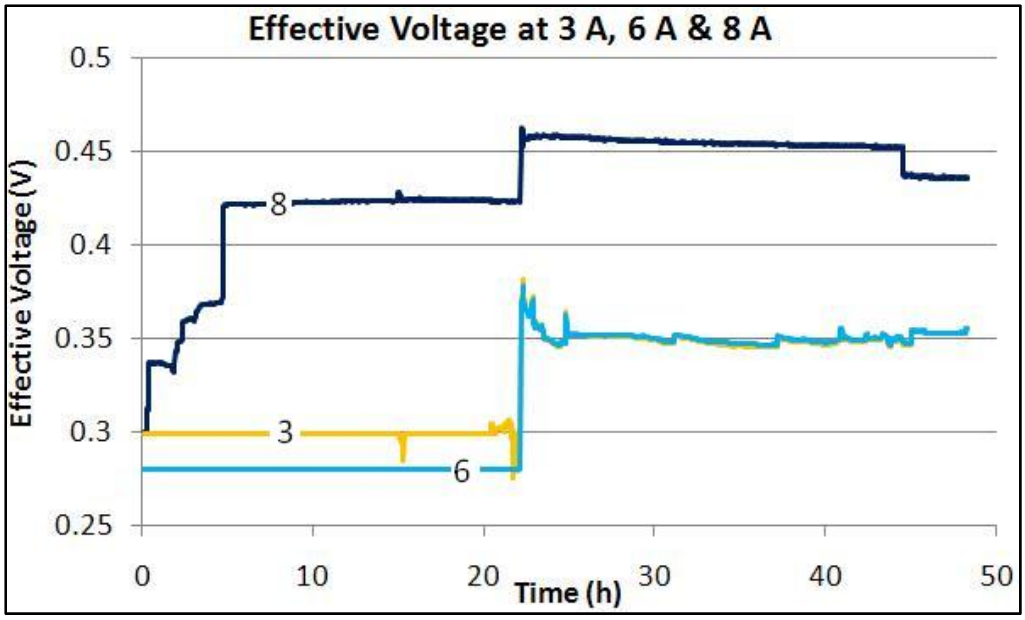

We can see that the maximum resistance was incurred at the onset of flooding, leading to the maximum effective voltage at all three locations. Even from this curve, it is obvious that location (8) was the first to incur flooding, and over time (3) and (6) also flooded.